TECHNISCHE
UNIVERSITÄT
WIEN

ICFO

MASTERTHESIS / DIPLOMARBEIT

Influence of Chirality in Energy Transfer of Fluorescent Molecules to Twisted Bilayer Graphene

by
Ambika Shorny
Mat.Nr.: 01648412

under the supervision of

Prof. Frank Koppens (ICFO)
Álvaro Moreno, Msc (ICFO)
ICFO – The Institute of Photonic Sciences

and

Prof. Gerhard Schütz (TU Wien)
Institute of Applied Physics - TU Wien

February 5, 2025

Abstract

Chirality plays a crucial role in chemical reactions and biological processes, highlighting the need for reliable enantioselective sensing techniques. Established chiroptical sensing methods, such as circular dichroism, are limited by low sensitivities due to weak light-matter interactions. To overcome this, sensing methods based on local enhancements of chiral light-matter interactions have been proposed. We explore a novel approach to enantiomeric sensing based on resonant energy transfer from fluorescent molecules to twisted bilayer graphene (TBG). With both systems being intrinsically chiral, the efficiency of energy transfer is expected to depend on the chirality, leading to enhanced transfer and thus a measurable stronger reduction of the molecule's lifetime for matched chiralities. We perform numerical simulations of the electric-magnetic interaction between a chiral molecule and TBG, leading to dissymmetries comparable with theoretical calculations. Although the simulations do not resolve the discrepancy between experiment and theory, they provide promising insights into the distance dependence, potentially enabling longer-ranged chiral interactions. Furthermore, we present a sample that allows the reproduction of experimental findings and potentially enables the first measurements of the angle dependence of energy transfer to TBG and the influence of chirality.

Deutsche Kurzfassung

Die Chiralität spielt bei chemischen Reaktionen und biologischen Prozessen eine entscheidende Rolle, was den Bedarf an zuverlässigen enantioselektiven Sensortechniken deutlich macht. Etablierte chiroptische Sensormethoden, wie z. B. der Cirkulardichroismus, sind aufgrund der schwachen Licht-Materie-Wechselwirkungen durch geringe Sensitivität limitiert. Um dies zu überwinden, wurden Sensormethoden vorgeschlagen, die auf einer lokalen Verstärkung der chiralen Licht-Materie-Wechselwirkungen basieren. Wir untersuchen einen neuartigen Ansatz für die Enantiomer-Sensorik, der auf der resonanten Energieübertragung von fluoreszierenden Molekülen auf Twisted Bilayer Graphene (TBG) beruht. Da beide Systeme intrinsisch chiral sind, wird erwartet, dass die Effizienz des Energietransfers von der Chiralität abhängt, was zu einem verstärkten Transfer und damit zu einer messbar stärkeren Verkürzung der Lebensdauer des Moleküls bei gleicher Chiralität führt. Wir führen numerische Simulationen der elektrisch-magnetischen Wechselwirkung zwischen einem chiralen Molekül und TBG durch, die zu Dissymmetrien führen, die mit theoretischen Berechnungen vergleichbar sind. Obwohl die Simulationen die Diskrepanz zwischen Experiment und Theorie nicht auflösen, bieten sie vielversprechende Einblicke in die Abstandsabhängigkeit, die möglicherweise chirale Wechselwirkungen mit größerer Reichweite ermöglichen. Darüber hinaus stellen wir eine Probe vor, die die Reproduktion experimenteller Ergebnisse und möglicherweise die ersten Messungen der Winkelabhängigkeit der Energieübertragung auf TBG und des Einflusses der Chiralität ermöglicht.

Contents

1 Introduction

A system is chiral when it is not superimposable on its mirror image or, more generally, when it lacks inversion symmetry. Examples of chiral systems include human hands and circularly polarized light, as shown in figure 1.1. The concept of chirality is fundamental across various fields, including physics, chemistry, and biology; in particular it is a fundamental feature of life-sciences, as most biological molecules on earth are homochiral and amino acids primarily occur left-handed [1]. Chirality plays a significant role in chemical reactions and biological processes in which both participants are chiral. More than half of the drugs currently in use are chiral products and their enantiomers frequently exhibit distinct biological activities such as differences in pharmacology or toxicology [2]. Therefore the ability to discriminate between enantiomers is a highly sought-after capability in the chemical and pharmaceutical industries.

To be able to distinguish between enantiomers a chiral probe is required. The two manifestations of the same chiral system have the same physical properties, unless they interact with another chiral system. An example is the interaction of chiral molecules with circularly polarized photons having a different response to right or left circularly polarized light; that is known as optical activity [3]. A common way to characterize these differences is through dissymmetry factors. First introduced in 1930 as the anisotropy factor [4], this dimensionless parameter quantifies the difference in response to circularly left and right polarized light. Circular Dichroism (CD) has a dissymmetry factor defined as the difference normalized by the total absorption $g_{\mathrm{CD}} = \frac{A_+ - A_-}{\frac{1}{2}(A_+ + A_-)}$ where A_+ and A_- are the absorption of left- and right-circularly polarized light, respectively [3]. Similarly, for circularly polarized luminescence (CPL), $g_{\mathrm{CPL}} = \frac{I_+ - I_-}{\frac{1}{2}(I_+ + I_-)}$ quantifies the difference in the luminescence intensities, I_L and I_R, for left- and right-circularly polarized light [5]. The magnitudes of CD and CPL are both typically small for chiral molecules, since it scales with the ratio of molecular size to wavelength, expressed as $g \sim a/\lambda$, which is intrinsically small with $g \leq 10^{-4}$ to 10^{-2}, for visible light [6].


mirror plane
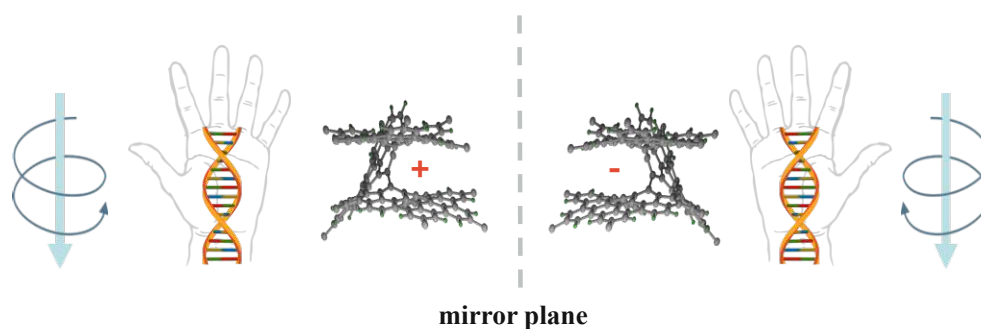
Figure 1.1: *Example of chiral systems. The two mirror images represent the two enantiomers or chiralities. Examples include human hands, inspiring the terms left- and right-handed, or chiral molecules, distinguished as '+' or '-' in this work. Another simple example is a (DNA) helix, as well as circularly left- or right-polarized light.*

Weak light-matter interactions limit the sensitivity of established chiroptical sensing methods such as CD. To address this challenge, various enhancement strategies have been proposed, including chiral and achiral plasmonic structures and metamaterials [7, 8]. These approaches usually deposit molecules on a prepared surface, which locally enhances the light-molecule interaction through micro- or nanostructures.

As these strategies are based on local enhancements, they require precise positioning or thick layers of molecules. An ideal platform for chiral sensing combines high sensitivity with tunability and spatial uniformity [6].

In this work, we propose a different approach for enantioselective sensing based on energy transfer between twisted bilayer graphene (TBG) and chiral fluorescent molecules [6, 9]. Whereas many sensing techniques rely on the enhancement of the interaction between the molecule and light, this project studies the chiral interaction between the molecule and another chiral system, in this case a thin material that acts as an energy acceptor. The fluorescence of the molecules is quenched by TBG, and the magnitude of quenching is selectively dependent on chirality. The modified, enhanced decay rate can be measured via time-resolved photoluminescence, thereby revealing the molecular chirality.

1.1 Graphene, TBG and Energy Transfer
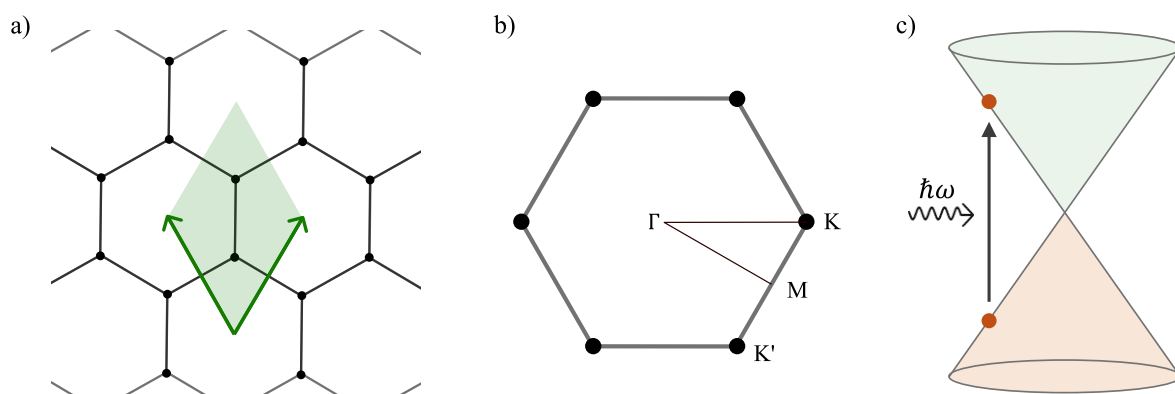
Figure 1.2: *a) Real space crystal structure of graphene. The green arrows indicate the lattice vectors and the shaded region is the unit cell of the honeycomb lattice. b) Brilloin zone of graphene with the Dirac-points K, K' as well as the M and Γ point. c) Sketch of the band structure of graphene around the K points and possible optical transition. An electron from the valence band (orange) is excited into an empty state in the conduction band (green), by the absorption of a photon with energy $E = \hbar\omega$.*

Graphene, first isolated in 2004 [10], is a two-dimensional material consisting of a single layer of carbon atoms arranged in a hexagonal lattice. This corresponds to a triangular Bravais lattice, where the basis contains two (equivalent carbon) atoms, as shown in figure 1.2 a). The electronic band structure of graphene shows a linear dispersion around the K and K' points of the Brilloin zone, depicted in b), up to energies on the order of one eV. This gives rise to cones located at the K points, called Dirac cones, because the dispersion resembles the energy of ultrarelstivistic particles that are described by the massless Dirac equation [11]. At the Dirac points K, K', the density of state (DOS) is zero and graphene is a zero-bandgap material. Due to the linear dispersion of graphene given by

$$E = v_F \hbar |\mathbf{k}| \tag{1.1}$$

where $v_F \approx 10^6$ m/s is the Fermi velocity and $\mathbf{k}$ the wave vector, it's optical conductivity close to the charge neutrality point only depends on universal values [12]

$$\sigma = \frac{e^2}{4\hbar} \tag{1.2}$$

where e is the elementary charge and $\hbar$ the reduced Planck constant. σ is independent of microscopic parameters, which is valid while the linear dispersion approximation holds and associated with transitions in the linear regime (see figure 1.2 c)). The transmittance, absorption, and reflection, can also be expressed using fundamental constants. For instance, using the fine structure constant $\alpha = \frac{e^2}{\hbar c}$, the transmittance is given by T $\approx 1 - \pi\alpha$ [13]. With negligible reflectance, the absorption A $\approx \pi\alpha \approx 2.3\%$, which has been experimentally verified [12].

1.1.1   Energy Transfer

A fluorescent molecule can be either excited resonantly (from and to the vibrational ground state of an electronic transition) or non-resonantly involving higher vibrational modes. Vibrational relaxation to the vibrational ground state and subsequent radiative decay (with typical lifetimes of 1-10 ns) to the ground state leads to red-shifted fluorescence [14]. The fluorescence of the molecule is quenched in the presence of a suitable energy acceptor, offering an alternative to the emission of photons, for the decay of the system. Förster resonance energy transfer (FRET) is a non-radiative process in which energy is transferred resonantly from an excited state of a donor (D) to an acceptor (A). The rate of energy transfer $\Gamma_{D\to A}$ normalized by the decay rate in absence of the acceptor Γ_0, follows the relation [14]

$$\frac{\Gamma_{D\to A}}{\Gamma_0} = \left(\frac{d_0}{d}\right)^6 \tag{1.3}$$

where d_0 is the Förster radius, for a distance d which is much smaller than the wavelength. The d^{-6} distance dependence applies to FRET between two point-like systems. However, when a dipole or molecule interacts with an extended system, the distance dependence generalizes to $d^{-(n+3)}$, where $n = 3, 2, 1, 0$ corresponds to the dimensionality of the acceptor system: 0D, 1D, 2D, or 3D [15]. For instance, the FRET distance dependence changes to d^{-3} for a bulk (3D) system, whereas for a 2D system, such as graphene, it follows d^{-4}. Furthermore, the energy transfer to graphene exhibits a universal distance scaling governed by the fine structure constant α.

1.1.2   Twisted Bilayer Graphene

Graphene itself is an achiral system. This changes, however, when placing two layers with a relative angle θ and a finite separation a, on top of each other [16]. TBG's opposite chirality is reached by changing the twist angle to $-\theta$ (or flipping the top and bottom layer) as it is illustrated in figure 1.3 a). In figure 1.3 c) the bandstructure of TBG is shown. It arises from coupled Dirac cones from the individual layers [17] with a shift between the corresponding dirac points in momentum space [18]. Band anticrossings at the intersection lead to saddle points and van Hoove singularities in the density of states (DOS). The main peak in the optical absorption of TBG corresponds to transitions at the saddle point from the lowest

a)

b)

c)

d)
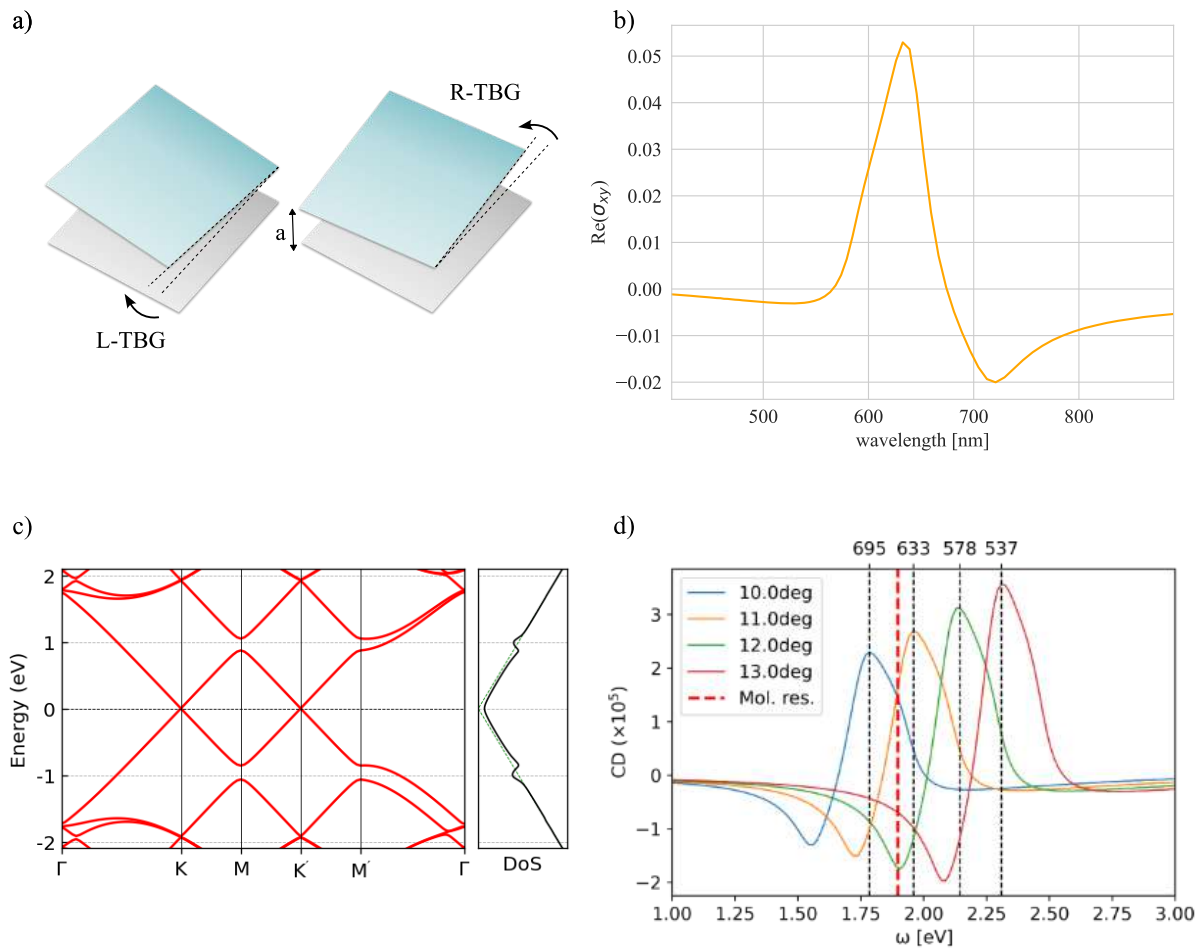
Figure 1.3: *a) TBG as a structurally chiral sytsem. The two layers are separated by a distance a, the top layer is rotated by either + or -θ with respect to the bottom one, resulting in L-TBG or R-TBG. b) Chiral optical conductivity σ_{xy} of graphene. c) Bandstructure (left) and density of states (DOS) of TBG. d) Wavelegnth dependent CD for different twist angles θ.*

valence to the second conduction band [17]. TBG has been shown to exhibits strong CD relative to its thickness, with a tunable peak energy that depends on the twist angle [19].

This dependence is a result of the corresponding transition which is determined by the relative position of the Dirac cones, originating from the individual layers, which depends on the twist angle, as illustrated in figure 1.4. With the geometrical construction shown in a), we can write $sin(\theta/2) \approx \theta/2 \approx \Delta k/2|K|$ for small angles θ, where Δk is the distance in momentum between the K points of the layers and $|K| = \frac{4\pi}{3b}$ is the magnitude of the K point vector, with b being the lattice parameter of graphene. With the linear dispersion of graphene (equation (1.1)), this results in [20]

$$\theta \approx \frac{3Eb}{\hbar v_F 4\pi} \tag{1.4}$$

which gives, in this approximation, a linear relation between the photon energy $E = \hbar\omega$ and the twist angle.
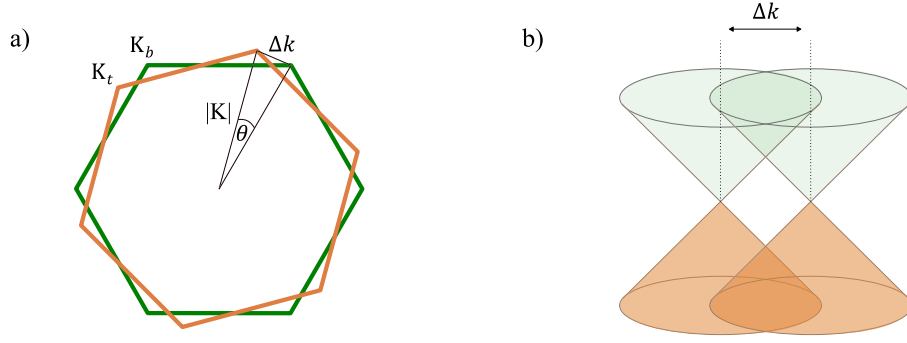
Figure 1.4: *a) Brilloin zone of the by θ relatively rotated graphene layers, resulting in a distance of the K points of the top (orange) and bottom (green) layer. b) Overlap of the Dirac cones of the individual graphene layers.*

To model the optical response of TBG we follow the theory [21] and define

$$\begin{pmatrix} J_x^{(1)} \\ J_y^{(1)} \\ J_x^{(2)} \\ J_y^{(2)} \end{pmatrix} = \begin{pmatrix} \sigma_0 & 0 & \sigma_1 & \pm\sigma_{xy} \\ 0 & \sigma_0 & \mp\sigma_{xy} & \sigma_1 \\ \sigma_1 & \mp\sigma_{xy} & \sigma_0 & 0 \\ \pm\sigma_{xy} & \sigma_1 & 0 & \sigma_0 \end{pmatrix} \begin{pmatrix} E_x^{(1)} \\ E_y^{(1)} \\ E_x^{(2)} \\ E_y^{(2)} \end{pmatrix} \tag{1.5}$$

where $J_x^{(i)}$ and $J_y^{(i)}$ represent the in-plane current densities, and $E_x^{(i)}$ and $E_y^{(i)}$ denote the corresponding in-plane electric fields for layer $i = 1, 2$, which are separated by a finite distance a. The main contribution to the conductivity tensor is given by the longitudinal conductivity σ_0, which corresponds to the in-plane conductivity within each layer. The covalent drag conductivity σ_1 generates a current by a field in the other layer, parallel to this field. In contrary, the Hall drag-like conductivity σ_{xy} leads to a current in the other layer, perpendicular to the field. Given the sign structure in equation (1.5), this response is not the same in the two layers and is thus related to the chiroptical properties of TBG. For example, consider an incident CPL beam perpendicular to the TBG surface. Owing to the finite distance a, there is a phase shift of the **E** vector between the fields in the two layers. Additionally, the chiral conductivity introduces a shift of the resulting currents, with the direction depending on the sign. This leads to a different response to circularly left and right polarized light and provides an intuitive understanding of CD in TBG. Upon changing the twist angle θ, $\sigma_{xy}(\theta) = -\sigma_{xy}(-\theta)$ reversing the sign of CD, while $\sigma_{0,1}(\theta) = \sigma_{0,1}(-\theta)$, for the same frequency ω [16, 21].

To model the chiral light-matter interaction of TBG, we use an effective (minimal) theory presented in reference [21]. By introducing magnetization, the non-local electric field description of equation (1.5) can be transformed into an effective local description that includes both electric and magnetic fields through electromagnetic coupling. The total in-plane magnetic moment (per unit surface) is given by

$$\mathbf{m}_\parallel = a\,\mathbf{j}_m \times \hat{\mathbf{z}} \tag{1.6}$$

where $\mathbf{j}_m$ is the difference between the current densities in the two layers $\mathbf{j}_m = \frac{1}{2}\left(\mathbf{j}^{(1)} - \mathbf{j}^{(2)}\right)$. In this description, it arises from a magnetic dipole density $\mathbf{m}_\parallel/a$, which uniformly fills the space between the layers.

From formula 1.5, we get $\mathbf{j}^{(1)}, \mathbf{j}^{(2)}$ and

$$\mathbf{j}^{(1)} - \mathbf{j}^{(2)} = (\sigma_0 - \sigma_1)\left(\mathbf{E}^{(1)} - \mathbf{E}^{(2)}\right) + \sigma_{xy}\begin{pmatrix} E_y^{(1)} + E_y^{(2)} \\ -E_x^{(1)} - E_x^{(2)} \end{pmatrix} \tag{1.7}$$

such that 1.6 becomes

$$\mathbf{m}_\parallel = \frac{a}{2}(\sigma_0 - \sigma_1)\left(\mathbf{E}^{(1)} - \mathbf{E}^{(2)}\right) \times \hat{\mathbf{z}} + \frac{a}{2}\sigma_{xy}\left(\mathbf{E}^{(1)} + \mathbf{E}^{(2)}\right). \tag{1.8}$$

We can rewrite the first part of the equation by using the maxwell equation $\nabla \times \mathbf{E} = -\frac{\partial \mathbf{B}}{\partial t}$. By assuming $\mathbf{B}(t) = \mathbf{B}_0\, e^{-i\omega t}$ we can write $\nabla \times \mathbf{E} = i\omega\mathbf{B}$ where ω is the frequency. (Note that in this step a sign-convention of the fields is assumed.) With a finite difference approximation we can write $\mathbf{z} \times (\mathbf{E}_2 - \mathbf{E}_1) = i\omega a \langle\mathbf{B}_\parallel\rangle$, where $\langle\mathbf{B}_\parallel\rangle$ is the avarage magnetic field between the layers, which we can directly compare with equation 1.8. For the second part of the equation, we write the average of the electric field as $\langle\mathbf{E}_\parallel\rangle = \frac{\mathbf{E}^{(1)} + \mathbf{E}^{(2)}}{2}$ so that we obtain the expression

$$\mathbf{m}_\parallel = a\sigma_{xy}\mathbf{E}_\parallel + i\omega\frac{a^2}{2}(\sigma_0 - \sigma_1)\mathbf{B}_\parallel \tag{1.9}$$

where we approximated the fields by their values at the center of the bilayer. Similarly by defining a surface polarization density $\mathbf{p}_\parallel$ by $\mathbf{j}^{(1)} + \mathbf{j}^{(2)} = -i\omega\mathbf{p}_\parallel$ one can write

$$\mathbf{p}_\parallel = -2\frac{\sigma_0 + \sigma_1}{i\omega}\mathbf{E}_\parallel - a\sigma_{xy}\mathbf{B}_\parallel. \tag{1.10}$$

Standard volume magnetization and polarization are given accordingly by $\mathbf{M} = \mathbf{m}_\parallel\delta(z)$ and $\mathbf{P} = \mathbf{p}_\parallel\delta(z)$ with $\delta(z) = ((a/2)^2 - z^2)/a$ and $\mathbf{D} = \epsilon_0\mathbf{E} + \mathbf{P}$, $\mathbf{H} = \mu_o^{-1}\mathbf{B} - \mathbf{M}$ with the vacuum permittivity ϵ_0 and permeability μ_0. Equations 1.9 and 1.10 represent constitutive equations of the form

$$\mathbf{D} = \epsilon\mathbf{E} - a\sigma_{xy}\mathbf{B} \tag{1.11}$$

$$\mathbf{H} = \mu^{-1}\mathbf{B} + a\sigma_{xy}\mathbf{E} \tag{1.12}$$

that couple the electric and magnetic fields. $\mathbf{D}$ is the electric displacement, $\mathbf{H}$ the magnetic field, $\mathbf{B}$ the magnetic induction, ϵ the relative permittivity and μ the relative permeability. The equations have a form similar to the constitutive relations

$$\mathbf{D} = \epsilon\mathbf{E} + \xi\mathbf{H} \tag{1.13}$$

$$\mathbf{B} = \mu\mathbf{H} + \zeta\mathbf{E} \tag{1.14}$$

where ξ and ζ are dimensionless magnetoelectric parameters, that are commonly used to describe bi-isotropic media. That is, a class of media that twists the polarization of transmitted light [1].

For the circular dichroism of TBG, we consider incident circularly polarized light with polarization $\mathbf{u}_\pm = (\mathbf{x} \pm i\mathbf{y})/\sqrt{2}$. The transmission and reflection amplitudes are calculated in [21] using the induced polarization and magnetization (equations (1.10) and (1.9)), resulting in

$$t_\pm = \left[1 - \frac{\sigma_0 + \sigma_1}{\epsilon_0 c} \mp \frac{\omega a \sigma_{xy}}{\epsilon_0 c^2} \right] \mathbf{u}_\pm \tag{1.15}$$

and

$$r_\pm = \left[\frac{\sigma_0 + \sigma_1}{\epsilon_0 c} \right] \mathbf{u}_\pm \tag{1.16}$$

The absorption $A_\pm = 1 - R_\pm - T_\pm$ is determined by the reflection and transmission coefficients $R_\pm = |r_\pm|^2$ and $T_\pm = |t_\pm|^2$ respectively. This leads to the following CD of TBG:

$$CD = \frac{A_+ - A_-}{2(A_+ + A_-)} = \frac{\mathrm{Re}(\sigma_{xy})}{2\,\mathrm{Re}(\sigma_0 + \sigma_1)} \frac{\omega a}{c}. \tag{1.17}$$

Since the conductivities $\sigma_0(\theta, \lambda)$, $\sigma_1(\theta, \lambda)$ and $\sigma_{xy}(\theta, \lambda)$ are a function of the twist angle, the resulting CD in TBG is not only wavelength-dependent but also depends on the twist angle θ. As a result, the main CD peak of TBG is tunable with the twist angle, an example is shown in figure 1.3 d).

1.2 Spontaneous decay and dipole approximation

In general, the description of spontaneous decay of an emitter requires a quantum electrodynamics (QED) description because spontaneous emission is understood as a purely quantum effect. However, for a two-level system in the weak-coupling regime, QED and classical theory yield the same result for the modification of spontaneous decay in an inhomogeneous environment [14]. This equivalence is summarized by the following relation

$$\frac{\Gamma}{\Gamma_0} = \frac{P}{P_0} \tag{1.18}$$

where on the left-hand side is the spontaneous decay rate Γ, which can be extracted from the experiment, divided by a reference value, for example the spontaneous decay of the emitter in vacuum Γ_0. P on the other hand, is the power dissipation by a radiating dipole, which can be treated according to classical electrodynamics, also divided by its vacuum value.

Accordingly, we can use the dipole approximation to model the fluorescence molecule. Since we are interested in the chiroptical properties, it is not sufficient to use only an electric dipole. Instead, these properties are well captured by a combination of electric and magnetic dipole moments with a relative phase of $\pm\frac{\pi}{2}$ [5] such that

$$\mathbf{d}_\pm = \pm i\mu + \mathbf{m}. \tag{1.19}$$

Parallel dipole moments emit light with a left circularly polarized component, while antiparallel moment emit light with a right-handed component. This can be easily understood by considering the fields emitted by the dipoles. The electric field generated by an electric dipole aligns with the orientation of the dipole, whereas for a magnetic dipole, the magnetic field of the electromagnetic wave is parallel to the dipole, resulting in an electric field perpendicular to it.

1.3 TBG as a platform for enantioselective sensing
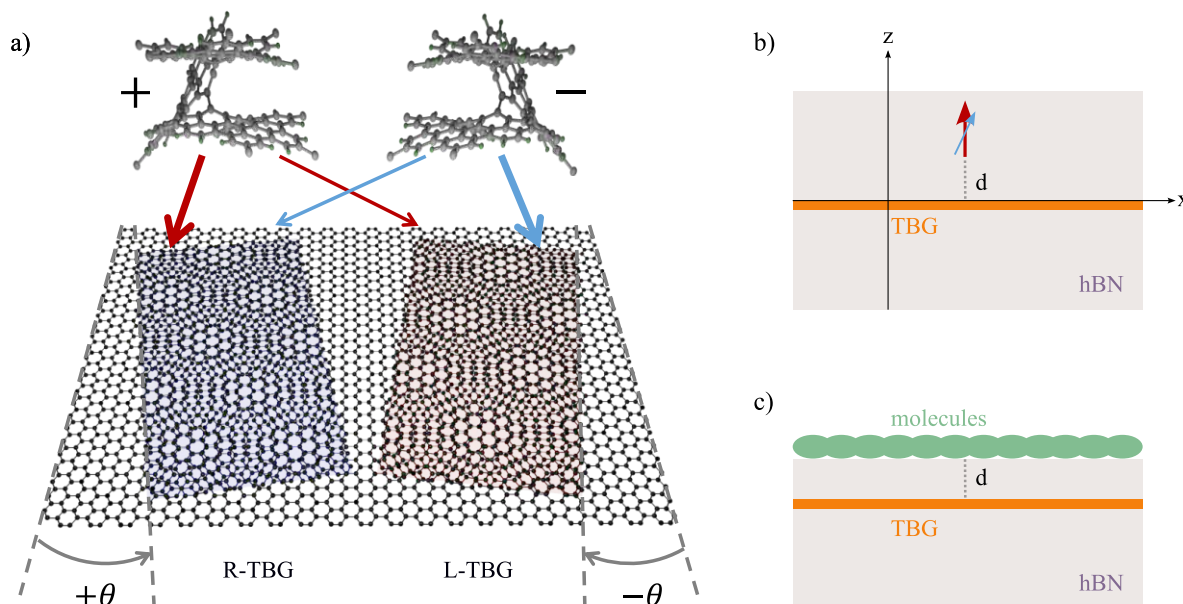
Figure 1.5: *a) Schematic energy transfer from molecules to TBG depending on the chiralitiy of both systems. Indicated by a thicker arrow, it is more efficient for matched chiralities. b) Sketch of the configuration used for theoretical calculations. c) Sketch of the experimental configuration of the sample. TBG is encapsulated in hexagonal boron nitride (hBN) with a layer of molecules on top. In both cases d denotes the distance between the molecules and TBG.*

As an atomically flat, structurally chiral material with tunable circular dichroism (CD), twisted bilayer graphene (TBG) is well suited for studying chiral energy transfer, with TBG acting as the energy acceptor. Consider a fluorescent molecule with optical transition energy $\hbar\omega$, described by its decay rate $\Gamma = \frac{1}{\tau}$, where τ is the lifetime. When placed close to TBG, the molecule can transfer energy resonantly to the bilayer structure instead of emitting a photon. As discussed earlier, the twist angle can be adjusted so that the peak absorption and CD of TBG matches the molecular transition energy. This results in a modified decay rate of the molecule, depending on the energy transfer efficiency.

The molecules chosen for this project are Helical Bilayer Nanographenes (HBNG) [22]. Collaborators from the Claudia Felser group at the Max Planck Institute synthesized the molecules and calculated their chiroptical properties using densitiy functional theory (DFT). The main optical transition has a wavelength of $\lambda = 650$ nm (see Table 1), such that a twist angle of approximately $\theta = 11°$ matches the resonance well. This versatile approach can be adapted to other chiral molecules.

The energy transfer between the chiral molecule, which exhibits CPL, and TBG, which exhibits CD, depends on the chirality of both systems. As illustrated in figure 1.5 a) the energy transfer is more efficient for matched chiralities, leading to shorter lifetimes and higher decay rates Γ. The energy transfer can be separated into a chiral and an achiral contribution, where the latter is expected to be dominant. The modified decay rate

$$\Gamma = \Gamma_{\text{achiral}} \pm \Gamma_{\text{chiral}} \tag{1.20}$$

results in the quenching of both chiralities [6]. However, the opposite sign of the chiral contribution leads to enhanced quenching for matched chiralities compared with unmatched chiralities. This difference allows us to distinguish between these two cases.

Recently, the modification of the decay rate in this system was calculated in [9] by collaborators of the Marco Polini group at the University of Pisa. According to the relation in equations (1.18) and (1.19), the modified spontaneous decay is calculated as the irradiated power of the combination of electric and magnetic dipole moments with a distance d to TBG, as illustrated in figure 1.5 b). The power was calculated using the Green's function of the field reflected from the twisted bilayer structure. Apart from the vacuum contribution P_0, the total power has contributions from the reflected field, which has electric and magnetic components, with the first index describing the dependency on the electric or magnetic dipole moment and the second describing the reflected electric or magnetic fields:

$$P = P_0 + P_{e,e}^{\text{ref}} + P_{m,m}^{\text{ref}} + P_{e,m}^{\text{ref}} + P_{m,e}^{\text{ref}}. \tag{1.21}$$

with

$$P_{e,m}^{\text{ref}} = P_{m,e}^{\text{ref}} \tag{1.22}$$

and

$$P_{e,m}^{\text{ref}}(\mathbf{d}_\pm, \pm\theta) = -P_{e,m}^{\text{ref}}(\mathbf{d}_\pm, \pm\theta) = -P_{e,m}^{\text{ref}}(\mathbf{d}_\pm, \mp\theta) \tag{1.23}$$

where $\mathbf{d}_\pm$ denotes the parallel or antiparallel dipole moments and θ is the twist angle. Equation (1.23) represents the chiral contribution and has opposite signs for matched and unmatched chiralities. A dissymmetry factor is defined as follows

$$g = \frac{\Gamma_+ - \Gamma_-}{\Gamma_+ + \Gamma_-} = \frac{P_+ - P_-}{P_+ + P_-} \tag{1.24}$$

where the index refers to parallel or antiparallel dipoles, for a fixed substrate chirality.

1.4   Motivation and Content

Theoretical calculations result in a dissymmetry factor of $g \sim 10^{-4}$ for a distance between TBG and molecules of $d \approx 4$ nm, which is comparable to experiments. First results have already been obtained experimentally [6], showing the expected dissymmetry in the chiral interaction. Nevertheless, the dissymmetry factor obtained from the experiment is about $g \sim 0.1$ and thus exceeds the theoretical value by various orders of magnitude. The schematic experimental configuration of the sample is shown in figure 1.5 c). The TBG layer is encapsulated in hexagonal boron nitride (hBN), a dielectric layered material, which introduces a distance between TBG and the layer of molecules.

Despite showing the same expected effect in theory and experiment, the huge difference in the order of magnitude suggests that further understanding is needed. Simulations are a powerful tool for investigating the effect under idealized conditions, allowing us to study parameter variations, such as the dependence on TBG-molecule distance or orientation, which are difficult to access experimentally. Furthermore, simulations can help us deepen our understanding of the underlying mechanism. In this report, we show, that electromagnetic simulations are able to capture the chirality dependent energy transfer from molecules

to TBG. They do not resolve the discrepancy as they are close to agreement with theory, but give us interesting insights such as the distance dependence of the dissymmetry.

Due to challenging fabrication (of clean samples) and measurements, the experimental results have not yet been fully reproduced. We would like to go a step further in validating the findings by fabricating a new device. In addition to reproducibility, we are interested in varying experimental parameters, such as the angle dependence, which could be studied in a sample with areas of different twist angles, on the same sample.

The structure of this report is as follows: After an introduction to the topic, which includes a brief discussion about graphene, TBG and energy transfer (Section 1.1) and spontaneous decay (Section 1.2, as well as a description of the project on enantioselective sensing with TBG (Section 1.3), we proceed with a chapter on electromagnetic simulations (Chapter 2). It is organised in the following sections. First, the model used for simulations is introduced (Section 2.1), followed by an overview of the finite element method (FEM) and its application in COMSOL (Section 2.2). Before presenting the results of the final simulations (Section 2.4), preparatory simulation steps are discussed (Section 2.3). The experimental Chapter 3 is subdivided into two sections. The first discusses fabrication procedures, including exfoliation and stacking (Section 3.1), while the second focuses on the presentation and analysis of a specific sample (Section 3.2). The report concludes with a summary of the findings and an outlook on potential future steps (Section 4).

2 Simulations

2.1 Model

Before starting with simulations, we first need to think of a suitable model that is able to capture the effect of interest but simple enough to implement. To this end, we need to combine some considerations and approximations already made in the introduction. An overview of the simulation model is shown in figure 2.1.

We use the relation (1.18) between the spontaneous decay rate of an emitter and the power dissipation of a dipole, which allows us to perform classical electromagnetic simulations, to obtain the relative difference in spontaneous decay for the chiralities, which can be compared with measurements. To model the chiral molecule, we use the dipole approximation and equation (1.19).
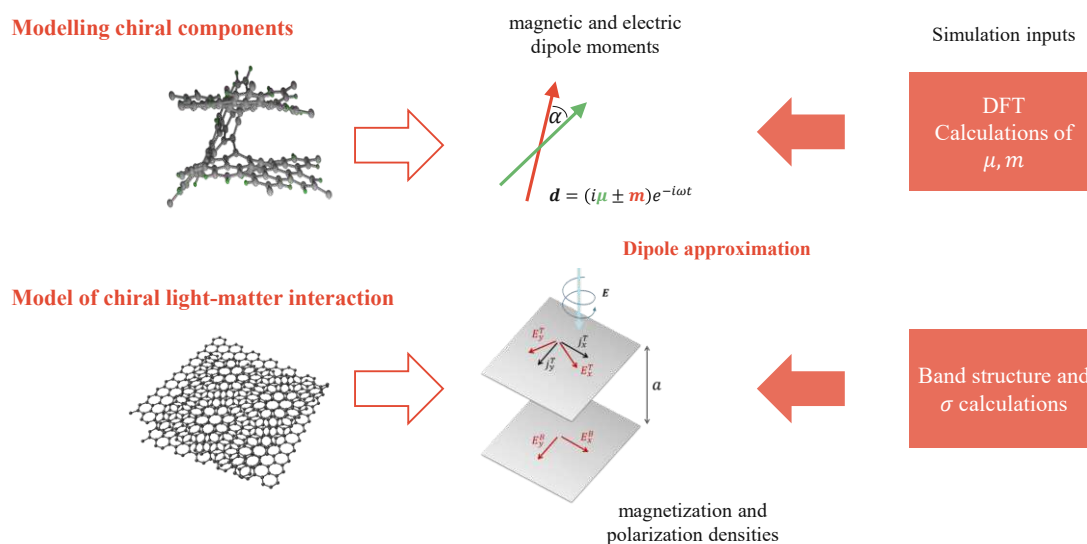
Figure 2.1: *Simulation model. We simulate the chiral molecule as a combination of electric and magnetic dipole moments μ and **m**. As simulation input we use DFT calculated magnitudes from table 1. As input for the TBG model, we use conductivities σ obtained from other simulations. In an effective model, magnetization and polarization densities are used to express constitutive equations that couple the electric and magnetic field.*

To model a real molecule, the magnetic and electric dipole moments can have arbitrary orientations with a relative angle α (see figure 2.1). Usually the magnetic moment is much smaller than the electric moment, such that the amount of circularly polarized light is only a small percentage of the overall emission. (The dissymmetry for strongly allowed transitions is about 10^{-3} [5].) The intrinsic dissymmetry factor of circularly polarized photoluminescence of a molecule is given by

$$g_{\text{CPL}} = \frac{4c|\mu||\mathbf{m}|\cos(\alpha)}{|\mu|^2 + c^2|\mathbf{m}|^2}.$$ (2.1)

It is an important value when considering the interaction of the molecule with TBG, however it should not be confused with the dissymmetry factor of the TBG-molecule system.

Table 1: Simulated chiroptical properties of the first transition of HBNG1 by DFT calculations for an isolated molecule and a molecule relaxed on hBN. For other transitions of HBNG1 see Appendix 6,7.

Parameter	Isolated molecule	relaxed on hBN
Wavelength (nm)	631.2	653.9
$|\mu|$ (10^{-30} Cm)	9.868	6.702
$|\mathbf{m}|$ (10^{-3} Am^2)	1.466	1.261
$\cos(\alpha)$	-0.243	-0.099
g_{CPL}	0.0048	0.0025

The emission properties of the specific molecules used in the project are summarized in Table 1, which serve as simulation inputs. In the DFT calculation, the molecule is either simulated isolated, which corresponds to a molecule in vacuum or relaxed on a substrate, in our case hBN. The chiroptical properties change slightly when the HBNG1 molecule is relaxed on hBN, for completeness simulations for both cases are performed. For simplicity, simulations are performed mainly with (anti)parallel dipoles and the effect of the angle is checked in a separate simulation.

To model TBG, we use the effective theory from [21] discussed in Section 1.1.2 with the constitutive equations (1.10) and (1.9). Using these equations we implement the TBG model and simulate its chiroptical properties. As simulation input, we use simulated values for the conductivities σ_0, σ_1 and σ_{xy}.

2.2   FEM and Comsol

In order to implement the model described in Section 2.1, we use the finite element method (FEM) for electromagnetic simulations. FEM is a method for numerically solving a partial differential equation (PDE) based on discretization. FEM theory has significantly developed over time, evolving into a robust framework used in diverse applications such as structural mechanics, transport phenomena, and electromagnetic simulations. For our project, we use the commercially available software COMSOL [23] and more specifically, its radio frequency (RF) module, that solves the electromagnetic wave equation in the frequency domain.

To better understand the solved equation, we start with the Maxwell equations in the frequency domain for a time harmonic field $\mathbf{E} = \mathbf{E}e^{i\omega t}$:

$$\nabla \times \mathbf{E} = -i\omega\mathbf{B} \tag{2.2}$$

$$\nabla \times \mathbf{H} = i\omega\mathbf{D} + \mathbf{j} \tag{2.3}$$

$$\nabla \cdot \mathbf{D} = \rho \tag{2.4}$$

$$\nabla \cdot \mathbf{B} = 0 \tag{2.5}$$

Where $\mathbf{E}$ is the electric field, $\mathbf{D}$ is the electric displacement, $\mathbf{H}$ is the magnetic field, $\mathbf{B}$ is the magnetic induction, $\mathbf{j}$ is the current density and ρ is the charge density. Multiplying the first equation by the inverse of the permeability μ^{-1} and applying $\nabla\times$ leads to

$$\nabla \times \mu^{-1}\nabla \times \mathbf{E} = -\nabla \times \mu^{-1}i\omega\mathbf{B}. \tag{2.6}$$

The current density is split into source and conduction current density $\mathbf{j} = \mathbf{j}_s + \mathbf{j}_c$ and we set $\mathbf{j}_s = 0$. Another assumption made, are linear constitutive relations

$$\mathbf{D} = \epsilon_0 \epsilon \mathbf{E} \tag{2.7}$$

$$\mathbf{B} = \mu_0 \mu \mathbf{H} \tag{2.8}$$

$$\mathbf{j}_c = \sigma \mathbf{E}. \tag{2.9}$$

With the vacuum permittivity ϵ_0, the permittivity ϵ, the vacuum permeability μ_0 and the vacuum wave number $k_0 = \frac{\omega^2}{c^2}$. After inserting equation 2.3 and the constitutive relations, we obtain

$$\nabla \times \mu^{-1}(\nabla \times \mathbf{E}) - k_0^2 \left(\epsilon_r - i \frac{\sigma}{\omega \epsilon_0} \right) \mathbf{E} = 0 \tag{2.10}$$

which is the wave equation solved by default in COMSOL. Note that another convention $\mathbf{E} = \mathbf{E}e^{-i\omega t}$ would lead to a '+' in the bracket term. In addition, note that the default equation is not suitable for simulating TBG, as the constitutive relations discussed in Section 1.1.2 are different from the linear ones assumed here.

We choose to use COMSOL instead of other established software such as Lumerical, which is generally well-suited for nanophotonic simulations, because it provides the possibility to access and modify almost all definitions and equations. This allows us to implement the constitutive equations 1.9 and 1.10 which couple the electric and magnetic fields. With this approach, COMSOL has already been successfully used for simulations of chiral media [24–26]. One could alternatively think of using a model in which the constitutive relations are reduced to an anisotropic ϵ. However, this only captures the electric field component but not the full constitutive relations, which is necessary to simulate the full electric-magnetic interaction between the two systems.

The two main simulation settings used in this project are shown in figure 2.2. Each geometric domain must be assigned material properties. To simulate the wavelength dependent CD, we use frequency dependent conductivities, calculated from the TBG band structure by an existing code in the group, which we import and interpolate. The configuration shown in a) simulates the absorption of graphene/TBG and consequently CD. The side length of the simulation box is 300 nm and the height 2400 nm. At the top and bottom there are 300 nm perfectly matched layers (PMLs) combined with scattering boundary conditions. The (periodic) excitation and absorption ports are located between PML and simulation domain. On the sides, we use periodic boundary conditions to simulate a plane wave. The slab in the middle represents graphene or TBG. Other shown domain separations are performed to specify the meshing. We use COMSOL's tetrahedral mesh and control the mesh size by setting the maximum element size for each domain or boundary. Then the software automatically builds a mesh with varying element sizes. Note that even if the geometry is symmetric, the generated mesh is most probably not. Because we are interested in dissymmetries such as the difference in response to circularly left and right polarized light, we want to force a symmetric mesh that can be created by copying meshing domains. We have observed that even if we apply a symmetric mesh to only one part of the total geometry, it already improves the
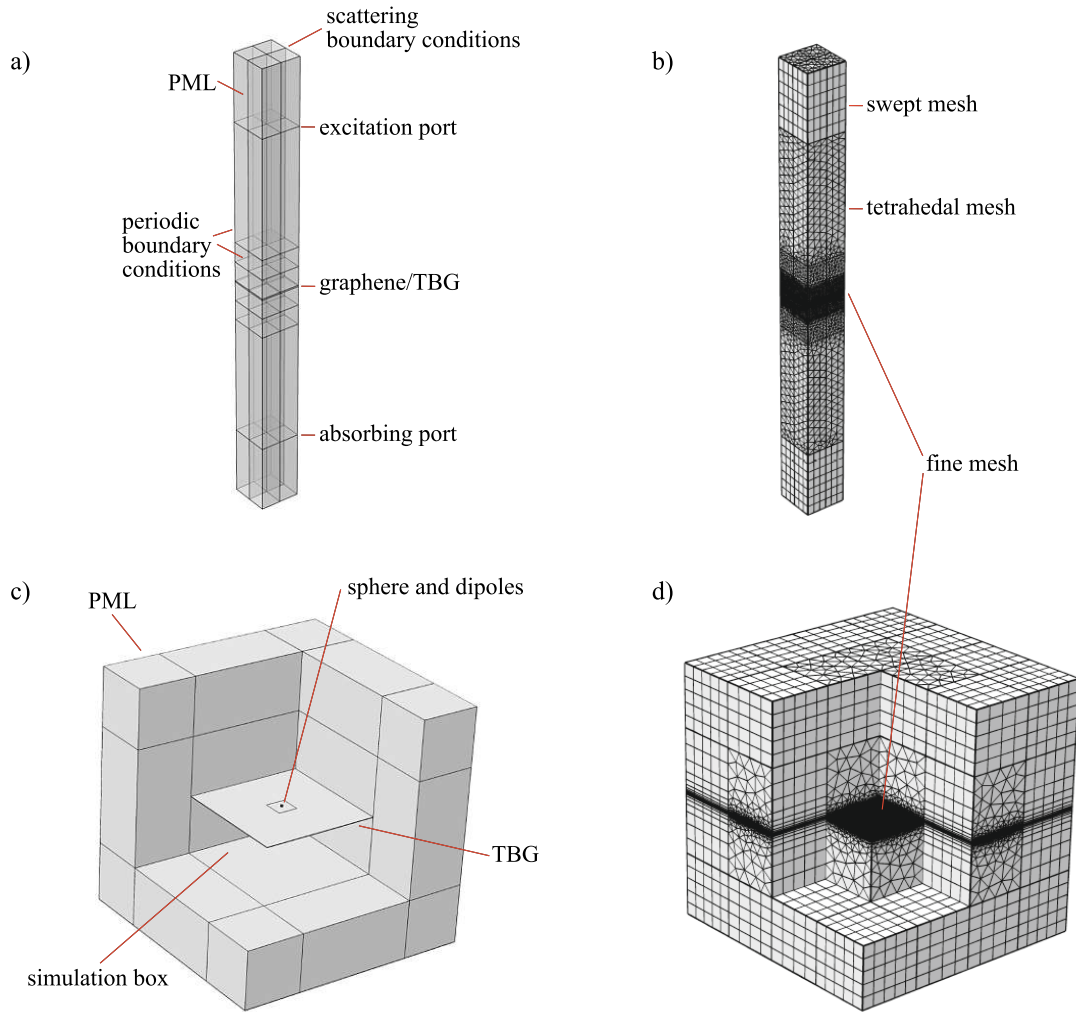
Figure 2.2: *The two main simulation geometries. a) The geometry used for simulating the absorption of a plane incident wave on TBG or graphene. On the top and bottom are perfectly matched layers (PML) and scattering boundary conditions. On the other sides there are periodic boundary conditions. b) Mesh of the geometry described in a), a finer mesh is applied around the slab in the middle of the simulation domain. b) Geometry of the final simulation configuration. A box surrounded by PML on all sides, TBG is simulated as a thin slab (with a modified wave equation). The point sources are surrounded by a small sphere used for poynting vector integration. d) Mesh of the geometry shown in c). Again finer meshes are applied around the sphere and TBG.*

simulated results. In the geometry shown in a), this is realized with the separations along the $x - z$ and $y - z$ planes. Domains of gradually finer meshes are applied around the thin slab, as indicated in b).

The simulation setting shown in c), a quadratic simulation box (600 nm side length), is used to simulate the modification of spontaneous decay. The box is surrounded by PML domains with a thickness of 300 nm, which corresponds to approximately half the wavelength. Within the simulation domain, we use a tetrahedral mesh, while a swept mesh with at least five elements is applied to the PML. In the middle of the box, the point sources, either electric or electric and magnetic dipoles, are placed. They are enclosed by a sphere ($r = 1$ to 4 nm). To calculate the irradiated power, we use COMSOL's surface integration tool for poynting vector integration. At $z = -d$, where d is a varying distance, is the surface of the material, either a thin slab of graphene/TBG or aluminum filling the lower half space of the simulation domain.

Around the sphere surface distance, which is small compared to the simulation box, again domains are specified for finer and symmetric meshes.

For TBG simulations, we modify the wave equation only in the corresponding domain. After enabling the equation view, one can access the equations and definitions and all modifications should be performed in a consistently. After comparing equation 1.10 with equation 2.10, we define the material property σ corresponding to the first term of $\mathbf{p}_\parallel$ as

$$\sigma_{\text{TBG}} = \begin{pmatrix} 2(\sigma_1 + \sigma_0)\frac{\sigma_{\text{qu}}}{d_{\text{TBG}}} & 0 & 0 \\ 0 & 2(\sigma_1 + \sigma_0)\frac{\sigma_{\text{qu}}}{d_{\text{TBG}}} & 0 \\ 0 & 0 & \sigma_\perp \end{pmatrix} \tag{2.11}$$

where $\sigma_{\text{qu}} = \frac{2e^2}{h}$ is the conductivity quantum (required because $\sigma_0, \sigma_1, \sigma_{xy}$ are given in units of σ_{qu}), d_{TBG} is the thickness of the TBG slab and $\sigma_\perp$ is the out-of-plane conductivity, which is set to zero in most simulations. We use the second term of equation 1.10 and equation 1.9 to modify the in-plane equations

$$p_{x,y} = -d_{\text{tbg}}\sigma_{xy}\frac{\sigma_{\text{qu}}}{d_{\text{tbg}}}B_{x,y} \tag{2.12}$$

$$H_{x,y} = \mu_0^{-1}B_{x,y} - a\sigma_{xy}\frac{\sigma_{\text{qu}}}{d_{\text{tbg}}}E_{x,y} - i\omega\frac{a^2}{2}(\sigma_0 - \sigma_+)\frac{\sigma_{\text{qu}}}{d_{\text{tbg}}}B_{x,y} \tag{2.13}$$

$$\frac{dH_{x,y}}{dt} = \mu_0^{-1}\frac{dB_{x,y}}{dt} - i\omega a\sigma_{xy}\frac{\sigma_{\text{qu}}}{d_{\text{tbg}}}E_{x,y} - i\omega\frac{a^2}{2}(\sigma_0 - \sigma_+)\frac{\sigma_{\text{qu}}}{d_{\text{tbg}}}\frac{dB_{x,y}}{dt} \tag{2.14}$$

Because only predefined expressions can be used we set $\frac{dE}{dt} = i\omega E$ in $\frac{dH_{x,y}}{dt}$. For out-of-plane relations we use

$$p_z = 0, \tag{2.15}$$

$$H_z = \mu_0^{-1}B_z, \tag{2.16}$$

$$\frac{dH_z}{dt} = \mu_0^{-1}\frac{dB_z}{dt}. \tag{2.17}$$

These modifications correspond to a modification of the wave equation to

$$\nabla \times \mu^{-1}\nabla \times \mathbf{E} = \frac{(\omega^2\epsilon_0 - i\omega(\sigma_0 + \sigma_1))\mu^{-1}\mathbf{E} + i\omega\mu^{-1}a\sigma_{xy}(\mathbf{B} - \nabla \times \mathbf{E})}{\mu_0^{-1} + i\omega\frac{a^2}{2}(\sigma_0 + \sigma_1)}. \tag{2.18}$$

2.3 Simulation Steps

Simulations provide valuable insights and are a powerful tool to complement theoretical calculations and experiments, even for complex problems that cannot be solved analytically or are challenging to realize experimentally. However, the quality of the simulated results depends heavily on the model and its numerical implementation.

To ensure that our simulated results are not merely numerical noise and to verify aspects of our simulation model, we begin with simulations of simpler systems that can be compared with theory. This approach allows us to refine parameters, such as the mesh and boundary conditions. To this end, we focus on the essential aspects relevant to the final simulations. Specifically, we address the modification of the spontaneous decay of a dipole in an inhomogeneous environment and its distance dependence of both, bulk and 2D systems. We aim to capture chiroptical properties, focusing on both the chiral dipole and, in particular, the twisted bilayer.

2.3.1 Dipole near a planar interface
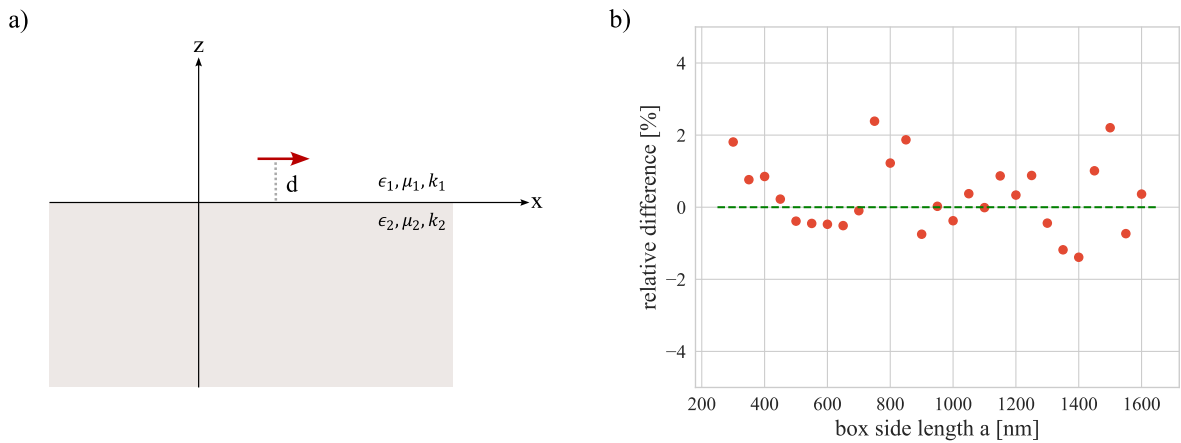
Figure 2.3: *a) Sketch of a dipole oriented along the x-axis with distance d to a planar interface. b) Variation of the relative difference between simulations results and theory equation* (2.19) *with the box side length a.*

A well-studied example of the modification of the spontaneous decay rate is the electric dipole near a planar interface. A detailed theoretical description of this problem can be found in [14]. Using a formalism based on Green's functions for the reflected field, the authors derived

$$\frac{P}{P_0} = 1 + \frac{3}{4} \int_0^\infty \mathrm{Re}\left\{ \frac{s}{s_z} \left[r^s - s_z^2 r^p \right] e^{2ik_1 d s_z} \right\} ds \tag{2.19}$$

for a dipole oriented along the x-direction and thus parallel to the interface. The radiated power is directly related to the decay rate according to equation 1.18. The perpendicular (superscript s) and parallel (p)
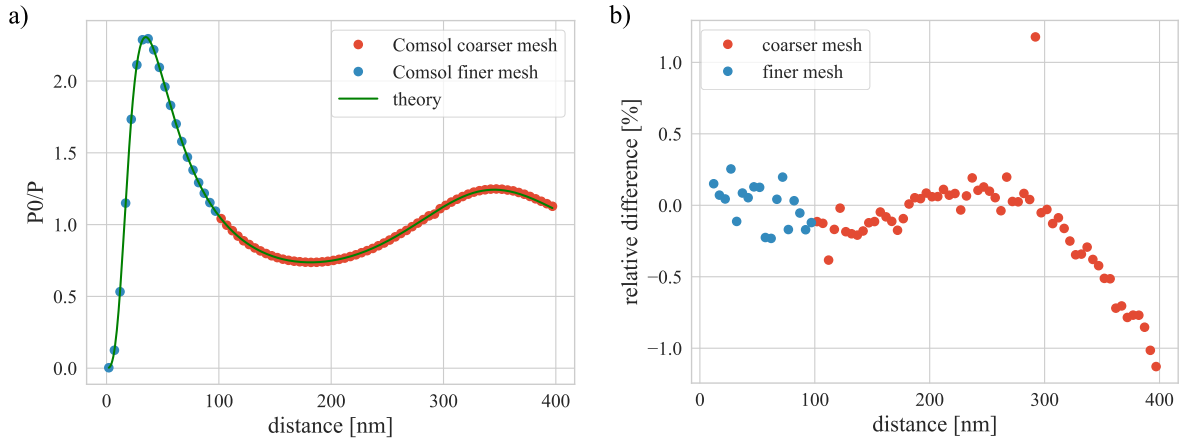
Figure 2.4: *a) Dipole radiation of an electric dipole close to an aluminum surface. Simulation results are compared to theory. b) The relative difference between simulation and theory. With a finer mesh for shorter distances, the deviations are below 0.5 %.*

reflection coefficients are given by

$$r^s = \frac{\mu_2\sqrt{1-s^2} - \mu_1\sqrt{\frac{k_2^2}{k_1^2} - s^2}}{\mu_1\sqrt{1-s^2} - \mu_2\sqrt{\frac{k_2^2}{k_1^2} - s^2}} \tag{2.20}$$

$$r^p = \frac{\epsilon_2\sqrt{1-s^2} - \epsilon_1\sqrt{\frac{k_2^2}{k_1^2} - s^2}}{\epsilon_1\sqrt{1-s^2} - \epsilon_2\sqrt{\frac{k_2^2}{k_1^2} - s^2}} \tag{2.21}$$

where subscript $i = 1, 2$ denotes the two regions separated by the interface, as illustrated in figure 2.3 a). In the general case the regions have relative permittivity ϵ_i, permeability μ_i and wave number $k_i = \frac{\omega}{c}\sqrt{\epsilon_i\mu_i}$. For simplification, the abbreviations $s = k_\rho/k_1$, where k_ρ is the radial component of k, and $s_z = \sqrt{1 - s^2}$ are used. The irradiated power by the dipole in vacuum is given by $P_0 = \frac{|\mathbf{d}|^2\omega k^3}{12\pi\epsilon_0\epsilon}$.

We simulate the dipole in vacuum with $\epsilon_1 = 1$, $\mu_1 = 1$, near an aluminum interface characterized by $\epsilon_2 = -32.607 + 8.4143i$ and $\mu_2 = 1$. The dipole frequency is defined as $\omega = \frac{2\pi c}{\lambda}$ where the wavelength is $\lambda = 600$ nm. Note that, according to equation 2.10, the imaginary part of the permittivity in COMSOL has to be implemented as conductivity $\sigma_2 = 8.4143\omega\epsilon_0$. For comparison with theory, we use the same parameters for the numerical integration of equation 2.19.

The simulation setup is similar to that described in Section 2.2 and shown is figure 2.2. The simulation box is meshed with a maximum element size of $\lambda/7$ whereas the interface boundary has a finer mesh with an element size of up to $\lambda/30$. The finest mesh, with a maximum element size of 0.5 nm, is applied to the surface of the sphere, which has a radius of 1 nm and is used for Poynting vector integration.

In contrast to issues encountered at the beginning, the simulated result using the described setting remains largely unchanged under variations in box size. Figure 2.3 b) shows the relative difference between the simulated P/P_0 and the theoretical value (for $d = 32$ nm). Here, P_0 is simulated as the dipole

radiation in the same simulation box but without the aluminum interface. Figure 2.4 a) shows P_0/P as a function of the distance between the dipole and the interface, comparing COMSOL simulations with the theoretical results (equation (2.19)). Using the coarse mesh described earlier leads to significant deviations from the theory for small distances, with large relative differences

$$\frac{\left(\frac{P_0}{P}\right)_t - \left(\frac{P_0}{P}\right)_s}{\left(\frac{P_0}{P}\right)_t} \tag{2.22}$$

between the results obtained by theory $\left(\frac{P_0}{P}\right)_t$ and simulation $\left(\frac{P_0}{P}\right)_s$. To better resolve the region between the dipole and the interface, we use a finer mesh (maximum element size of 2 nm) in a squared area (side length of 150 nm) around the dipole. With this finer mesh, the relative difference between the simulation and theory is reduced to below 0.5 % for small distances, which are particularly relevant for the final simulations (see figure 2.4 b)).
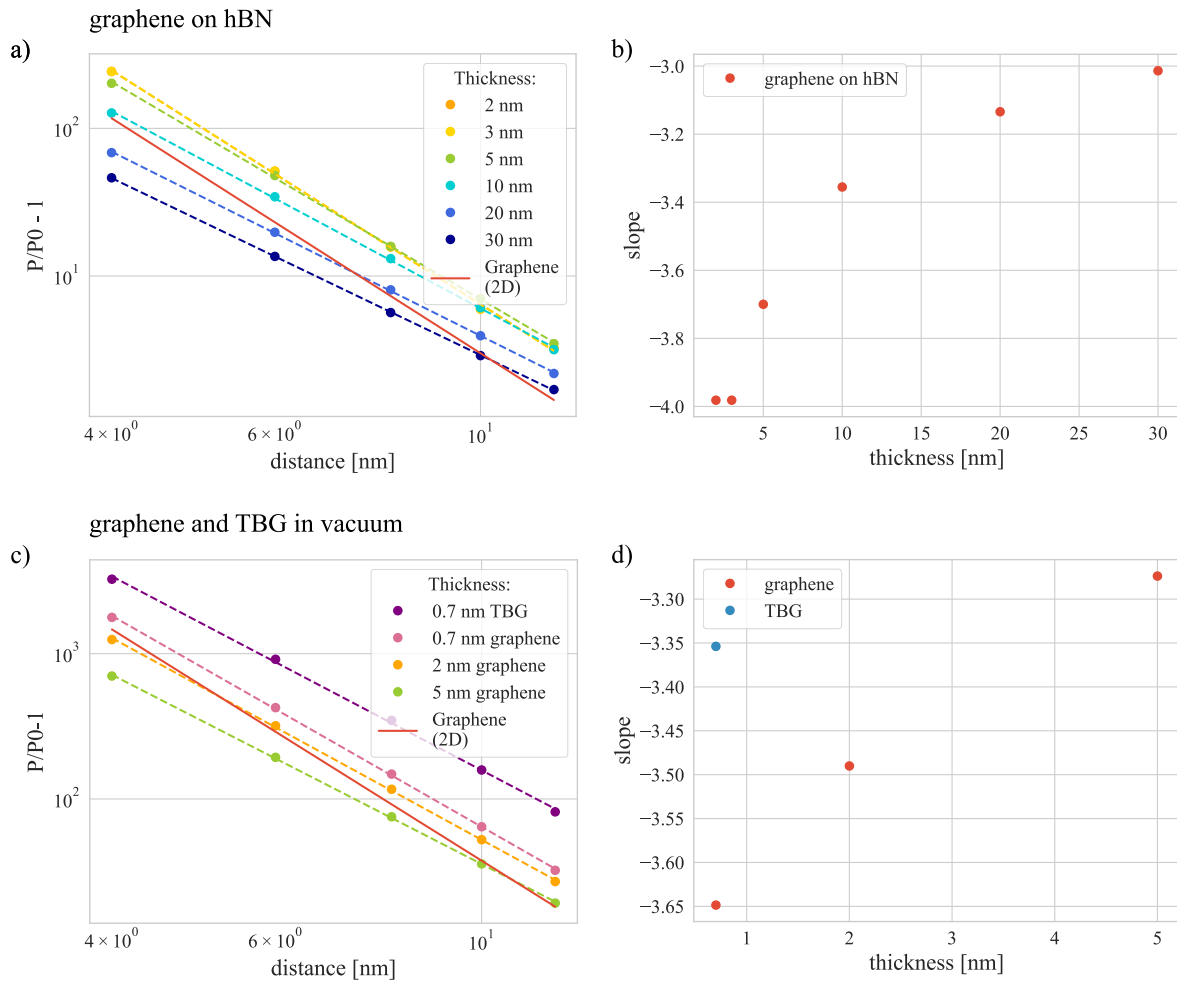
2.3.2   Dipole near Graphene

In Section 2.1, we have seen that the distance dependence of energy transfer for small distances below ~ 20 nm from a point-like system depends on the dimensionality of the energy acceptor. In the previous section we discussed a point dipole near a bulk material, such that the distance dependence in this range behaves like d^{-3}.

Although the three-dimensional nature of TBG is essential for its chiral properties (as it distinguishes between the top and bottom layers), its thickness of only 0.7 nm makes it effectively, like graphene, a 2D material. To capture its low dimensionality, graphene is often simulated as a surface current [27]. However, our model requires the simulation of TBG as a 3D slab to enable modifications of the wave equation within this domain. Simulating a slab with a thickness of less than 1 nm, which is much smaller than the other simulation dimensions, can be challenging. Therefore, we investigate whether larger thicknesses t, with a corresponding renormalized conductivity σ/t can adequately capture the 2D behavior of energy transfer. Following a previous study [15], we simulate an electric dipole near graphene. This study found a universal distance scaling for the modified decay rate

$$\frac{\Gamma_g}{\Gamma_0} = 1 + \frac{9\alpha}{256\pi^3(\epsilon+1)^2}\left(\frac{\lambda}{d}\right)^4 \tag{2.23}$$

where ϵ represents the substrate's relative permittivity, we set either $\epsilon = 1$ to compare with simulations of graphene in vacuum or $\epsilon = 4.98$ to simulate graphene on hBN. In the latter case, we start with a relatively thick slab of $t = 30$ nm and gradually decrease the thickness to 2 nm, as shown in figure 2.5 a). Using a linear fit of the logarithm of $P/P_0 - 1$ (indicated by the dashed line in a)), we extract the distance dependence from the fitted slope, as shown in b). All simulations are performed at distances between 4 nm and 12 nm. For thick slabs, the slope approaches -3, consistent with the bulk case. With decreasing thickness, the slope approaches the 2D case with slopes close to -4. For graphene on hBN, we observe this behavior already for thicknesses of 3 and 2 nm.

Figure 2.5: *Power dissipation (left) of a dipole near graphene on an hBN substrate (top) or in vacuum (bottom). Graphene is simulated as a 3D slab with varying distance t and conductivity σ/t. On the right, the corresponding slopes of the fitted curves (shown as dashed lines on the left) are shown. Dots correspond to simulated results and the solid red line is the theoretical value of equation 2.23*

For graphene in vacuum (c and d), the slope for a 2 nm thick slab is -3.49, deviating from the expected -4. To address this, we reduce the thickness further to 0.7 nm which corresponds to the thickness of TBG (about twice the thickness of graphene) and find a slope of -3.65 closer to the 2D case. For comparison, we also simulate the slab with the implemented model of TBG which results in a slope of -3.35. While the distance dependence does not perfectly follow d^{-4}, the behavior aligns with that expected for an energy-accepting thin material.

When comparing the fitted lines to the solid red line, which represents the theoretical spontaneous decay function near graphene (equation (2.23)), we observe a clear offset, even when the slopes are in good agreement. This discrepancy might arise because equation (2.23) is an approximation and is not fully comparable to our simulations. For our final goal of simulating a dipole near TBG, the relevant aspect of this simulation step is to determine a valid slab thickness for simulating a 2D system. A slab thickness below 5 nm, which achieves a slope approaching -4, appears sufficient to capture the appropriate distance dependence of the energy transfer.

2.3.3   Chiral Dipole

Until now, we have focused on the radiation properties of an electric dipole, corresponding to emitters such as fluorescent molecules. However, to account for the chiroptical properties of a chiral molecule, we must consider a combination of electric and magnetic dipole moments with a relative phase of $\frac{\pi}{2}$ (see 1.19). In COMSOL, this can be implemented by defining two point sources located at the same geometrical point. Note that in the RF module, one defines the electric current dipole moment which is the derivative of the dipole moment, $\mu e^{i\omega t}$. Consequently, by specifying $\mu_{\text{current}} = i\omega\mu$ as a real number, a phase of $\frac{\pi}{2}$ is inherently introduced relative to the magnetic moment which is also defined as a real number.
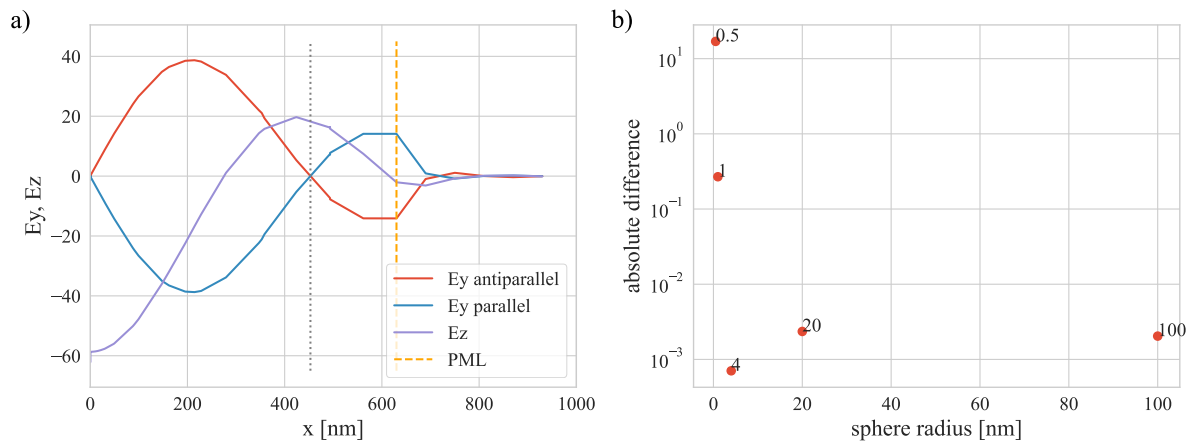
Figure 2.6: *a) Electric field components irradiated by a chiral dipole* $\mathbf{d} = \pm i\mu + \mathbf{m}$ *oriented along the x-axis. b) Absolute difference of* P_0 *for parallel and antiparallel oriented electric and magnetic dipoles, for differt sphere radii used for poynting vector integration.*

For most chiral molecules, including HBNG1, the magnetic dipole moment is significantly smaller in magnitude than the electric dipole moment, resulting in only a small fraction of the radiated field being circularly polarized, as described by the dissymmetry factor g_{CPL} (equation (2.1)). The power dissipation in vacuum for the two dipoles is given by the superposition of their individual contributions. For equal contributions to the total power,

$$P_0 = \frac{\omega^4}{12\pi\epsilon_0 c^3}\left(|\boldsymbol{\mu}|^2 + \frac{|\boldsymbol{m}|^2}{c^2}\right) \tag{2.24}$$

the magnetic dipole moment must satisfy $|\mathbf{m}| = c|\boldsymbol{\mu}|$. For this case, we plot the electric field of the two dipoles oriented along the x-axis in vacuum in figure 2.6 a). The y-component of the electric field exhibits opposite signs for (anti)parallel dipoles. Due to the $\frac{\pi}{2}$ phase difference, we expect a $\frac{\lambda}{4}$ phase shift between the y- and z-components, meaning that the zero-crossing of E_y (grey dotted line) should coincide with the maximum of E_z. The slight mismatch observed is due to the near field components. The box side length is twice the wavelength, $\lambda = 630$ nm, beyond which the field is damped in the PML domain (orange dashed line).

We can use P_0 to evaluate the quality of simulations, not only by comparing it to its theoretical value given by equation (2.24), but also by comparing its value for parallel and antiparallel dipoles. Ideally,

there should be no difference in P_0, as the radiated power in vacuum should not depend on their relative orientation. However, numerical noise will inevitably introduce small differences. For the final simulations, it is crucial to minimize these differences and to identify the noise level. There, we want to resolve the difference between the irradiated power of the two cases, caused by the inhomogeneous environment.

As before, we calculate the power by integrating the surface of a sphere. According to Poynting's theorem we should obtain the same result, independent of the sphere size. In previous simulations of the electric dipole moment, a radius of 1 nm led to good results. However, for combined electric and magnetic dipole moments, small sphere sizes lead to issues, including unphysical results such as negative power. In figure 2.6 b) we compare the absolute difference $|P_0^{\text{para}} - P_0^{\text{antipara}}|$ for various sphere radii. The large differences for small radii are likely due to numerical inaccuracies, whereas the differences stabilize at around 10^{-2} to 10^{-3} for larger radii, which appears reasonable.

2.3.4   Circular Dichroism of TBG
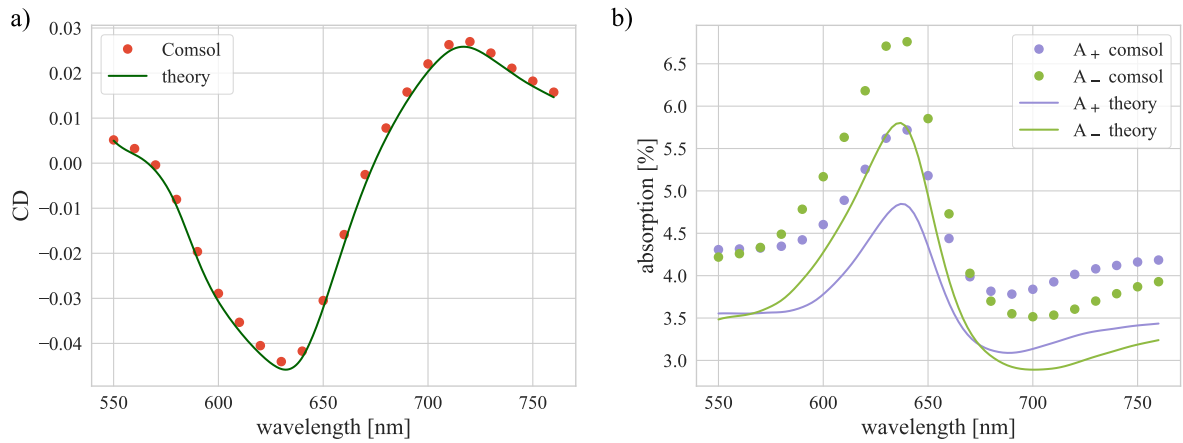
Figure 2.7: *a) Simulated circular dichroism (CD) of TBG, showing good agreement with the theoretical model from equation (1.17). b) Simulated absorption spectra for left-circularly A_+ and right-circularly A_- polarized light, compared to theoretical predictions.*

Having discussed the modification of spontaneous decay, its distance dependence and the radiation properties of a chiral dipole, the final puzzle piece to be explored before implementing our complete simulation model is the chiroptical properties of TBG. This step is crucial, as the implementation of the corresponding TBG model is particularly challenging and requires careful revision. This can be approached by simulating its CD and comparing the results with the theoretical formula in equation (1.17).

As a first step, we simulate the absorption of graphene by defining a slab with conductivity given by equation (1.2), which yields a value of approximately 2.15 %, which is close to the theoretical absorption of 2.3 %. For simulating CD, we calculate the absorption of circularly left and right polarized light and use the definition of

$$g_{\text{CD}} = \frac{A_+ - A_-}{2(A_+ + A_-)}. \tag{2.25}$$

Here, A_+ and A_- represent the absorption of left- and right-circularly polarized light, respectively. To simulate the absorption, we employ the simulation setup shown in figure 2.2 a) and described thereafter, which allows us to model a polarized plane wave interacting with the system.

TBG is simulated as a slab with a thickness of $t = 2\,\text{nm}$ which is compensated by dividing all conductivities by t. The constitutive equations (1.9) and (1.10) are implemented as described in equations (2.12)–(2.17). Since g_{CD} is expected to be small, σ_{xy} is multiplied by a factor of 100. According to equation (1.17), this results in an equivalent enhancement of the CD signal by a factor of 100. In figure 2.7 b) the simulated absorption for circularly left and right polarized light is shown. This is compared to theoretical values, obtained from equations (1.15) and (1.16):

$$A_\pm = \frac{2}{\epsilon_0 c}\left[\text{Re}(\sigma_0 + \sigma_1) \pm \frac{\omega a}{c}\,\text{Re}(\sigma_{xy})\right]. \tag{2.26}$$

We observe a clear offset between the theoretical and simulated absorption, which might arise from the slab thickness, the boundary conditions, or the applied multiplication factor. However, the shape is in good agreement and the offset is about the same for A_+ and A_-.

In figure 2.7 a) the simulated CD is compared to the theoretical prediction from equation (1.17). Apart from small deviations, the simulated and theoretical CD curves are in good agreement. We therefore conclude that this implementation of the model is valid for simulating the chiroptical properties of TBG.

2.4 Final Simulations

We have previously demonstrated the ability to simulate energy transfer to a low-dimensional material (Section 2.3.2). Additionally, we explored the chiroptical properties of both, a chiral dipole (Section 2.3.3) and TBG (Section 2.3.4). As a final step, we aim to integrate these components into a unified simulation. We use a simulation setting similar to that for the dipole near graphene but, instead of graphene, we implement the model of TBG in the slab domain. Furthermore, along with the electric dipole, we introduce a magnetic dipole to the system.

Table 2: Simulated power and dissymmetry (g) of a chiral dipole in vacuum and near TBG. Magnitudes are taken from table 1. P_0 represents the theoretical free space power, calculated according to equation (2.24) and serves as a reference. The simulated powers P_+ and P_-, which are expected to be equal in vacuum, along with the corresponding dissymmetry, provide an indication of the noise level in the simulations. g is evaluated according to equation (2.27). For the dipole near TBG, symmetric powers are observed for matched chiralities ('+'-molecule with R-TBG or '-'-molecule with L-TBG) and opposite chiralities, resulting in dissymmetry values with opposite signs.

	Vacuum	TBG	
		R - TBG	**L - TBG**
P_0 [nW]	$8.653180 \cdot 10^{-4}$		
P_- [nW]	$8.541273 \cdot 10^{-4}$	2.3459	2.3639
P_+ [nW]	$8.541391 \cdot 10^{-4}$	2.3643	2.3455
g	$\sim 10^{-6}$	$+3.907 \cdot 10^{-3}$	$-3.907 \cdot 10^{-3}$

Our objective is to simulate the energy transfer and associated change in the spontaneous decay rate of a chiral molecule near TBG. We are particularly interested in how this differs for matched and unmatched

chiralities. To allow a comparison with experiment and theory, we use a dissymmetry factor as introduced in Section 1.3:

$$g = \frac{\Gamma_+ - \Gamma_-}{\Gamma_+ + \Gamma_-} = \frac{P_+ - P_-}{P_+ + P_-} \tag{2.27}$$

which accounts for a fixed substrate chirality (L- or R-TBG). In our simulations, we can switch between the molecular enantiomers (+ and -) and the chirality of TBG.

In order to correctly interpret the simulation results, it is important to consider the noise level. For an estimation, we simulate the dissymmetry factor for a chiral dipole in vacuum by calculating P_+ and P_-. The magnitudes of μ and m are those of isolated HBNG1 (see Table 1) with $\lambda = 630$ nm. According to equation (2.24) this leads to $P_0 = 8.65 \cdot 10^{-4}$ nW, as shown in Table 2. For the vacuum case, P_+ and P_- correspond to the simulated P_0 values for parallel and antiparallel dipoles, respectively. We observe that the simulated values are slightly smaller than the theoretical expectation, though they are similar to each other, with only minimal differences quantified by a dissymmetry factor of $g \sim 10^{-6}$.

To ensure that our results are above the noise level, we apply a multiplication factor to σ_{xy}, as was previously done for simulating CD. The results are presented in the right-hand columns of Table 2. Within the limits of numerical noise, a (+) dipole near R-TBG radiates the same power as a (-) dipole close to L-TBG. The same is true for the other two combinations. This symmetry is also reflected in the dissymmetry factor, which shows opposite signs for matched and unmatched chiralities. While this outcome aligns with theoretical expectations, it provides additional confidence in the accuracy of the simulations.

Table 3: *Dissymmetry factor g for different multiplication factors of σ_{xy}. More details are given in appendix table 8.*

Multiplication factor of σ_{xy}	$\cdot 10^3$	$\cdot 10^2$	$\cdot 10^1$	$\cdot 1$
g	$\pm 3.9 \cdot 10^{-3}$	$\pm 5.2 \cdot 10^{-4}$	$\pm 5.2 \cdot 10^{-5}$	$\pm 5.3 \cdot 10^{-6}$

Regarding the magnitude of the results, it is important to keep in mind that we applied a multiplication factor to σ_{xy}. According to the theoretical formula for CD, it is proportional to σ_{xy} which is consistent with our simulated results in Section 2.3.4. A similar behavior is expected for g, as theoretical work [9] shows that the chiral contribution to the radiated power $P_{\text{ref}}^{e,m}$, is also proportional to σ_{xy}. We repeat the same simulations with a gradually decreasing multiplication factor, as shown in table 3. Reducing the multiplication factor by an order of magnitude leads to a corresponding decrease in g. For the initial simulation with $\sigma_{xy} \cdot 10^3$, the dissymmetry of ± 3.9 differs from the other simulations, which consistently yield dissymmetries around ± 5.2. As a validation step, simulations are performed for all possible combinations, and the complete results are provided in the Appendix Table 8. The real result, shown in the rightmost column, represents the simulation without an additional multiplication factor. With $g \sim 10^{-6}$ it is about noise level. However, its consistency with other simulations suggests that the results are reliable.

We have chosen a specific twist angle of TBG, with its wavelength-tunable CD, such that the peak aligns with the molecular resonance. Now we want to look at the resulting wavelength dependence of g for 11° and assess how well it matches the resonance of HBNG1. Simulations were conducted for parallel
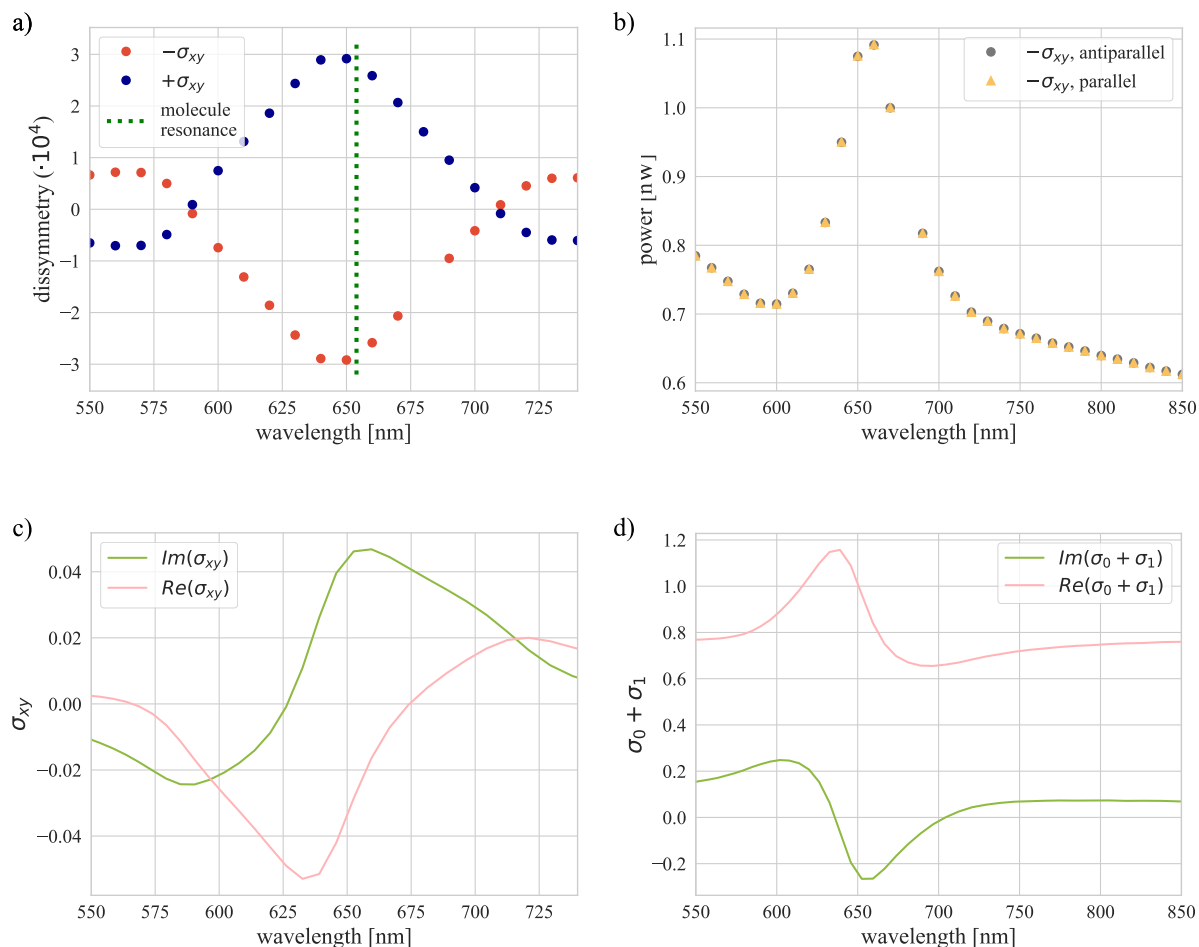
Figure 2.8: *a) The wavelength dependent dissymmetry factor shows a dip/peak around the same wavelength which matches well the molecuar resonance. It is symmetric for the two chiralities of TBG. It also matches the chiral conductivity σ_{xy} which is shown in c).b) Radiated power of the chiral dipole near TBG with $-\sigma_{xy}$, corresponding to a negative twist angle, shown for parallel and antiparallel dipoles. The peak near 650 nm corresponds to the maximum optical absorption associated with $\sigma_0 + \sigma_1$ plotted in d).*

and antiparallel dipoles oriented along the z-axis, with magnitudes corresponding to HBNG1 relaxed on hBN. In figure 2.8 b) the radiated power for the two enantiomers and same substrate chirality is shown. It exhibits a strong peak around the actual molecular transition energy. The data points for the two cases are very close, which indicates that the overall power is almost the same for the two cases and that the chiral component is very small in comparison. This allows us to compare the lineshapes to that of $\sigma_0 + \sigma_1$ shown in d), which represents the main contributions to the conductivity and, consequently, the optical absorption of TBG. Notably, there is good agreement between the positions of the peaks.

The small differences between the radiated power of parallel and antiparallel dipoles in figure 2.8 b) are reflected in the dissymmetry factor shown in 2.8 a). The red dots correspond to the case of $-\sigma_{xy}$ in b), the same analysis is applied to the other chirality of TBG with $+\sigma_{xy}$. These results are nearly perfectly symmetric about zero, with a peak/dip near the resonance of HBNG1. A comparison with the chiral conductivity σ_{xy}, plotted in c), shows that the peaks of its imaginary part and the dissymmetry factor align well.

24
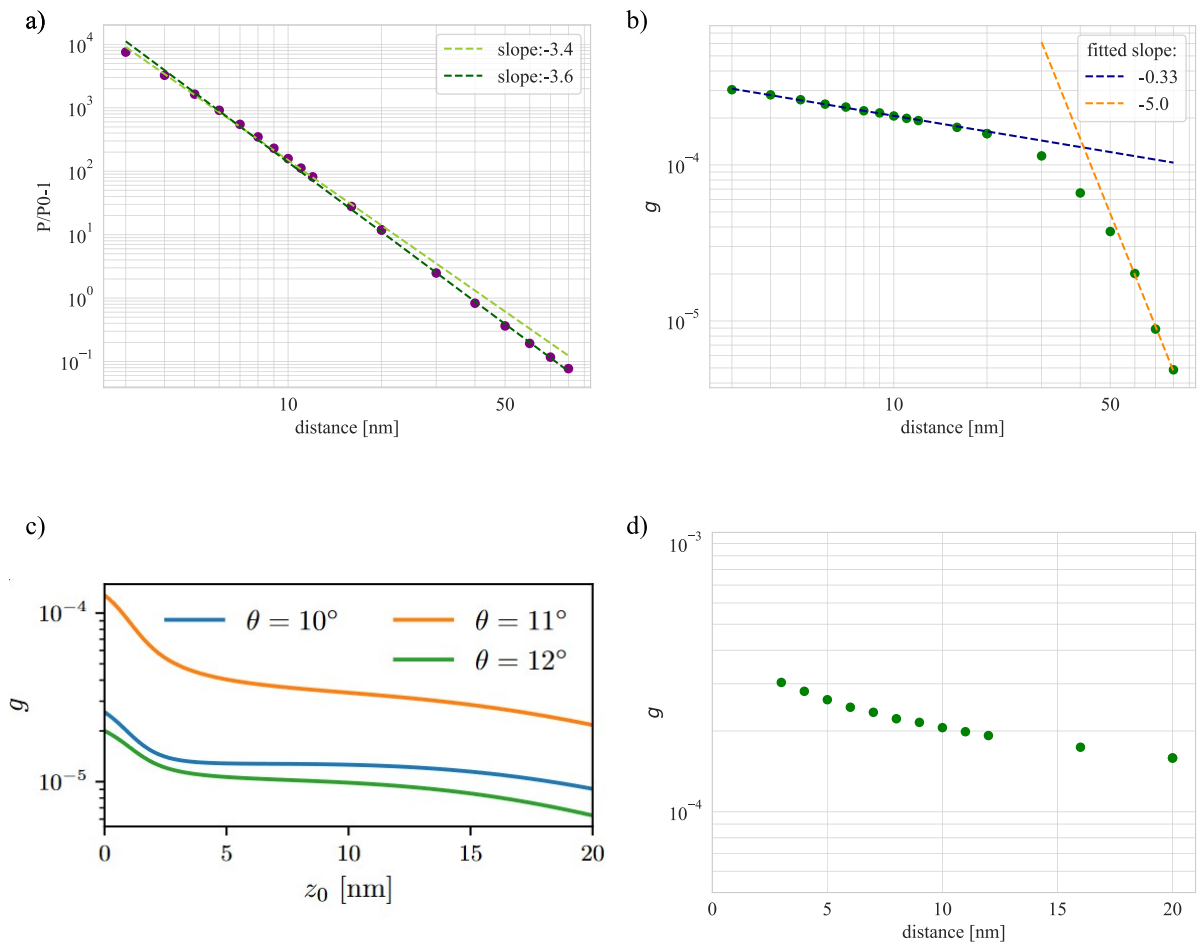
Figure 2.9: *a) Distance dependence of P/P_0-1 in a double-logarithmic scale with two fitted lines. The slopes indicate the distance dependence of two slightly different regimes, both of which are close to the expected value of -4. (b, c, and d) distance dependence of the dissymmetry factor g. b) The two clearly distinguishable regimes show slopes of approximately $-\frac{1}{3}$ and -5. c) Adapted from [9], showing g as a function of the distance (here called z_0) from theoretical calculations for different angles. d) Same as b), but presented in the same semi-logarithmic scale and range as c) for better comparison.*

We previously discussed that the distance dependence of energy transfer from a point source dipole to a two-dimensional material scales as d^{-4} for small distances. For the chiral dipole near TBG, we examine the slope of the logarithm of P/P_0 as it is shown in figure 2.9 a). The data suggests the possibility of two distinct trends; therefore we fit two separate lines for analysis. The slopes of -3.4 and -3.6, are close to -4. A similar analysis can be performed for the dissymmetry factor plotted as a function of distance in b). Here, two regimes are clearly identifiable, with a transition at around 40 nm. Below this distance, g decreases much more slowly than P/P_0, with a fitted slope of approximately $-1/3$. Remarkably, in this distance range, g does not even decrease by one order of magnitude whereas P/P_0 decreases by 2–3 orders of magnitude. This suggests that chiral interactions may persist over longer distances. At larger distances, g decreases much more rapidly. For a rough estimate, we fit the last three data points, obtaining a slope of -5. Although the extracted value might not be exact, the presence of two distinct regimes is clearly evident.

Theoretical work also examines the distance dependence, although we are limited to information extracted from the plot shown in c) along with their description, taken from [9]. For a better comparison, the distance dependence of g is shown in d) on the same semi-log scale as c). Our simulations do not cover the first region, up to 4 nm, owing to issues with small sphere sizes, as discussed in Section 2.3.3. The distance dependence in this region seems to be distinct from that in the subsequent region between ~ 4 nm and 20 nm. This second region, which is the only one directly comparable to our simulations, appears relatively flat and may correspond to the first regime identified in b). The second regime, observed at larger distances, cannot be compared directly. It is important to note that we compare our results with the orange line in c), corresponding to $\Theta = 11°$, which matches the conditions of the simulations. They observe a scaling of d^{-4} for longer distances, which coincides with the distance dependence of spontaneous decay. We observe a d^{-5} behavior for longer distances; however, this is a rough estimate resulting from fitting only three simulation points.
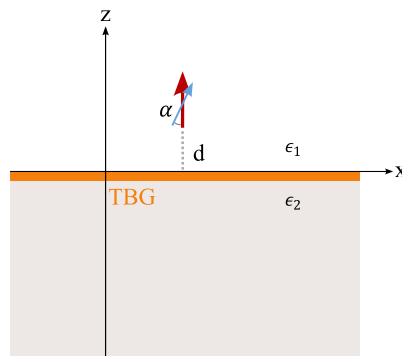
Figure 2.10: *Sketch of the simulation arrangement. In most simulations, the dipoles are oriented along the z direction and the angle between the magnetic and electric dipoles α is 0/180°. The relative permittivities ϵ_1, ϵ_2 are set to one for simulations of TBG in vacuum.*

Table 4: *Dissymmetry factor for TBG in vacuum, on a hBN substrate or in hBN. In figure 2.10 this corresponds to $\epsilon_1 = \epsilon_2 = 1$ in vacuum and $\epsilon_2 = 4.9$ or $\epsilon_1 = \epsilon_2 = 4.9$ in the other cases. Simulations are done for L-TBG with multiplication of σ_{xy} by 100. The distance between TBG and dipoles is d = 4 nm.*

substrate	hBN	half space hBN/vacuum	vacuum
g	$7.4 \cdot 10^{-4}$	$4.0 \cdot 10^{-4}$	$2.8 \cdot 10^{-4}$

Until now, we have considered TBG in vacuum. However in the experiment, TBG is encapsulated in hBN. The bottom flake supporting TBG is sufficiently thick to allow the lower half-space to be simulated as hBN with a relative permittivity of $\epsilon_2 = 4.9$. For illustration a sketch of the simulated arrangement is shown in figure 2.10. The top flake of hBN, which seperates the molecules from the chiral structure, is very thin (2–3 nm). In simulations, this would introduce an additional thin film, which is computationally costly, but feasible. The challenge, however, is that simulating dipoles directly on top of the hBN layer is not possible because of the method used to calculate the radiated power and issues with small sphere sizes, as discussed in Section 2.3.3. Theoretical calculations [9] assume $\epsilon_1 = \epsilon_2 = 4.9$ corresponding to the case

of TBG in hBN. A comparison of the simulation results for TBG in hBN, half space hBN and vacuum is presented in Table 4. g increases for $\epsilon_2 = 4.9$ compared to the vacuum case and reaches its maximum for $\epsilon_1 = \epsilon_2 = 4.9$. However, the dissymmetry remains within the same order of magnitude. Thus, we conclude that the hBN substrate does not considerably influence the results. This conclusion is further supported by simulations incorporating the top hBN layer with an additional 3 nm distance, which similarly yield a moderately increased dissymmetry.

Table 5: Comparison of the dissymmetry for parallel-oriented dipoles and dipoles enclosing an angle according to DFT calculations from table 1. Simulations were performed with σ_{xy} scaled by a factor of 100. The distance between TBG and dipoles is d = 4 nm.

	isolated HBNG1	**HBNG1 relaxed on hBN**
$g_\parallel$	$\pm 2.2 \cdot 10^{-4}$	$\pm 2.8 \cdot 10^{-4}$
$\cos(\alpha)$	-0.243	0.099
g_α	$\mp 1.0 \cdot 10^{-4}$	$\pm 2.7 \cdot 10^{-5}$

For simplicity, we assumed (anti)parallel dipoles in the simulations. According to the DFT calculations presented in Table 1, the two dipoles enclose a finite relative angle. For completeness, simulations are performed for the two cases of isolated HBNG1 and HBNG1 relaxed on hBN, both in vacuum with a multiplication factor of σ_{xy} of 100. This results in slightly smaller dissymmetry factors, as presented in Table 5. It is reasonable to expect that $g \sim \cos(\alpha)$ given that $g_{CPL} \sim \cos(\alpha)$ (see equation (2.1)). This relationship could explain the behavior observed for HBNG1 relaxed on hBN, although it does not strictly hold in the isolated case.

Another assumption in most simulations is that the dipoles are oriented along the z direction. Although the complex structure of HBNG1 makes a preferred molecular orientation on the sample conceivable, any arbitrary dipole orientation remains possible. Simulations with dipoles oriented along the x direction show no significant change in the dissymmetry, although changes in the absolute value of the radiated powers are observed. We conclude that the dipole orientation has at most minimal influence on g.

Considering that most simulations are performed with multiplication factors for σ_{xy}, the simulated magnitude of dissymmetry results in $g \sim 10^{-6}$ to $g \sim 10^{-7}$. One possible explanation for these smaller values compared to theoretical calculations is numerical dissipation. Additionally, this very small result might not be entirely surprising, as systems with already low intrinsic dissymmetry of $g_{CPL} \sim 10^{-3}$ and $g_{CD} \sim 10^{-4}$ are coupled. However, the much larger experimental results suggest that the simulations are unable to fully capture the effect.

3 Experimental

As previously mentioned, the first experimental results demonstrated a significantly greater effect than theoretical predictions suggested. Despite several attempts, replicating the experiment with the same quality level has not yet been achieved, primarily due to the challenges associated with fabricating clean samples. However, validating these experimental results by repeating the measurements on a different device is crucial. Beyond ensuring reproducibility, we aim to broaden our understanding by varying one of the parameters. This could be accomplished using a sample with regions of different twist angles, presented in Section 3.2.

As for the first results, the ideal sample contains two areas of TBG with identical twist angles but opposite signs, representing the two chiralities, along with a graphene region for reference. The main challenge is to obtain two homogeneous areas with the same twist angle. To protect the TBG layer and to control the distance between the molecule and TBG, it is encapsulated in hexagonal boron nitride (hBN). While the bottom hBN typically consists of a thick, large flake, the top hBN ideally has a thickness of less than 5 nm. Identifying and handling such thin hBN flakes is more difficult and complicates the transfer process. The fabrication process is discussed in more detail in the next section 3.1.

3.1 Fabrication

In the first fabrication step, we need to find all flakes that we need for the stack. This includes a thicker bottom hBN flake with a large, homogeneous area and a thin top hBN flake, ideally 2-3 nm thick, with a homogeneous region of at least 10-20 μm $\times$ 30-40 μm. For the TBG and graphene areas, a larger graphene flake is required, which will be cut into three pieces.
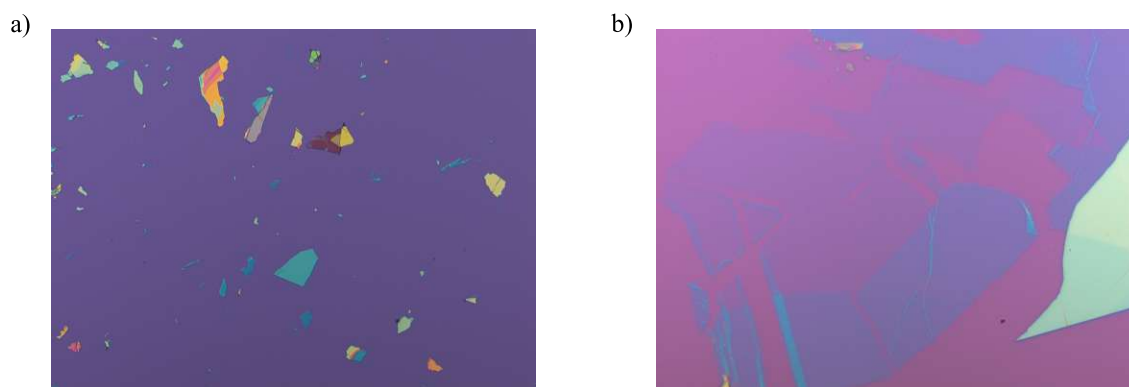

Figure 3.1: *a) Typical optical image of exfoliated hBN flakes with 5× magnification, showing flakes of different colors corresponding to different thicknesses. b) Example of a thin hBN flake with 50× magnification.*

All flakes are obtained through mechanical exfoliation of hBN crystals or graphite [28, 29]. For hBN, we use polydimethylsiloxane (PDMS) sheets to exfoliate. The crystal is fragmented by repeatedly attaching and detaching two PDMS sheets. Each repetition reduces the thickness and size of the crystals. Afterward, the flakes are transferred to a silicon wafer by gently placing the PDMS sheet onto the wafer

surface and peeling it off very slowly. The flakes that remain on the wafer are then examined under a microscope.

We use silicon wafers with a 285 nm thick SiO_2 layer which enables a better optical contrast. Under a microscope, interference effects cause flakes to appear in different colors depending on their thickness [30, 31]. This allows (with some experience) the selection of flakes just by optical inspection. An example of exfoliated hBN flakes is shown in figure 3.1 a). The blue-green flake in the lower middle, would be well suited as a bottom hBN flake. Thin flakes have a blue to purple tone, the thinner they are, the harder it is to distinguish them from the background. The thickness can be evaluated more accurately in an AFM measurement, which can also serve as a reference. In b) an example of a thin flake, suitable for use as top hBN, is shown.
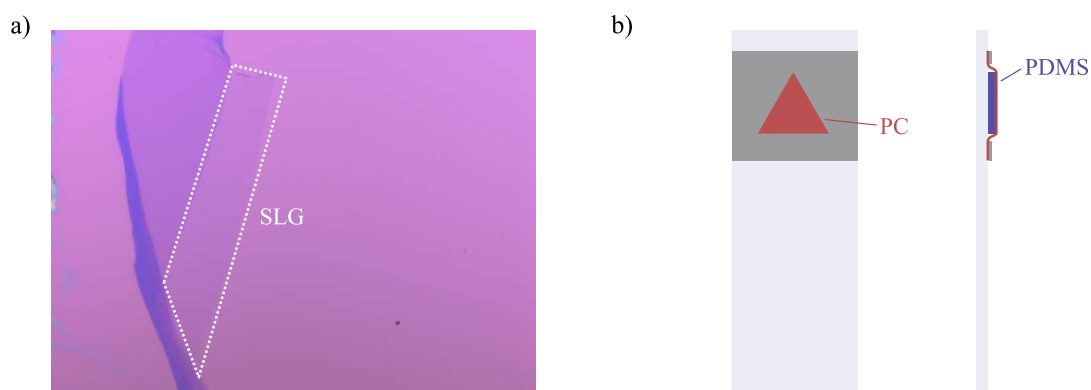

Figure 3.2: *a) Optical image of single layer graphene (SLG), attached to a few layer flake with 50× magnification. b) Sketch of a PC-stamp used for transfer.*

A similar procedure is applied for exfoliating graphene. Graphite is spread on a strip of scotch or blue tape and then copied onto a fresh piece of tape. This process is repeated until the graphite flakes on the tape appear sufficiently thin. Wafer chips are placed upside down on the piece of tape, which is placed on a hot plate at 100° C for several minutes. Subsequently, the chips are removed in a quick movement. Similar to hBN, graphite flakes can be examined under the microscope and graphene can be identified by its colour. Additionally the number of layers can be identified by examining the absorption, which is approximately 2 % for monolayer graphene. In figure 3.2 an optical image of graphene attached to a few layer flake, is shown.

To build a sample from the selected flakes, they are stacked on top of each other using a polymer stamp [32]. For the preparation of the stamps, we use a microscope slide. A triangle, cut out of PDMS, is placed on one side. A thin layer of polycarbonate (PC) is created by dropping a small amount of PC solution (chloroform) between two clean glass slides and quickly sliding them apart, leaving a uniform layer of PC on both slides. To transfer the PC onto the PDMS layer, a piece of scotch tape with a slightly larger triangular cutout is used. Similarly, a piece of double-sided tape with a matching triangular cutout is applied before placing the PC layer. The prepared stamp is then heated on a hot plate at 180° C, the melting point of PC, for some minutes, which flattens the PC film and ensures that there are no wrinkles.

Once all the flakes and the PC stamp are prepared, we can start with the stacking process. It is done using a transfer setup, which consists of a microscope, a rotational and translation stage for the sample and a translational stage for moving the stamp or an AFM-tip attached to a microscope slide, which is used for cutting. It is recommended to roughly plan the stack in advance. The top hBN is picked up first and should cover all graphene areas. Picking up graphene directly with PC is unlikely because it adheres strongly to the wafer, although it adheres more strongly to hBN than to SiO_2 [33]. If the graphene is not entirely covered, there is a risk that the top hBN will be dropped instead of successfully picking up the graphene. Ideally, the graphene flake is slightly larger so its edges can wrap around the hBN flake. To obtain the required three areas, both chiralities of TBG and single layer graphene (SLG), three pieces of the same graphene flake are needed. Using the same flake ensures that prior to rotating the pieces, they have the same crystallographic orientation [29]. This requires the flake to be cut, larger flakes have to be cutted additionally. With each cut, there is a risk of damage to graphene; thus fewer and precise cuts are preferable. Cuts with the AFM-tip can be performed horizontally or vertically, other directions are reached by rotating the sample. When planning the cuts, we should keep in mind that one larger piece and two smaller ones are required, with the latter intended for rotations of ± 11°. We also need to consider that we pickup the pieces after each other and need to prevent any interference, that is, unwanted touching of flakes in each step. An example of a cutted graphene flake and the picked up first piece with the according hBN flake is shown in figure 3.3.


a)

b)
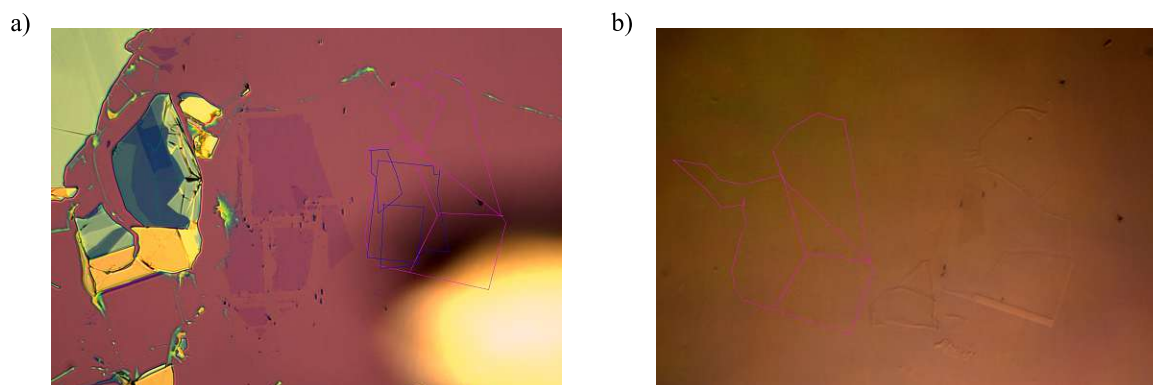
Figure 3.3: *a) Optical image of cutted graphene. On the right, a sketch of a possible stacking order is shown. The pink lines correspond to the top hBN flake, shown in b). b) image of a picked up top hBN and first graphene flake on the polymer stamp (right). On the left a skecth of the hBN flake is shown, which helps for aligning when picking up the other flakes. It is the same as the lower part of the flake shown in 3.1 b). We are interested in the thin part which is already hard to see in the optical image of the flake on the PC stamp.*

The stacking order is to first find all flakes and draw the top hBN. This sketch will later be used as a reference for cutting and alignment (see figure 3.3). In the next step, the graphene flake is cut according to the discussed considerations and, if necessary, the surrounding area is cleaned. We then start to pick up of the flakes with the polymer stamp. First the top hBN, followed by the graphene pieces. To obtain a relative angle, the sample stage must be rotated between the steps. Once the first graphene flake is picked up, the stamp is no longer moved. When all the flakes are picked up, the stack is dropped onto the bottom hBN.

For the transfer, the temperature of the stage is set to 100° C for better adhesion of the flakes on the stamp [34]. After positioning and orienting the flake, a clean spot near the tip of the stamp is selected for the first pick-up, otherwise the previously picked-up flakes on the stamp are aligned with the flake. While approaching, the exact positions should be checked and realigned if necessary. The stamp is slightly tilted, such that the front of the polymer can be moved over the sample. This should be done slowly and continuously, also when retracting for pickup. To drop the stack in the last step, the temperature is increased to 180° C. Instead of retracting directly, we wait until the PC has melted. The sample is then covered by a polymer film which is cleaned by placing it into chloroform for approximately 15 minutes.

In the final step of the sample preparation , the molecules are spincoated onto the stack, ideally resulting in a uniform and controlled deposition across the surface. HBNG1 molecules of both enantiomers are synthesised by our collobarators. We dilute them in toluene with a typical concentration of 1-10 μM/L and spincoat at 6000 rpm for one minute. The uniformity of the layer can be checked in the optical miscroscope and AFM, we aim for a uniform distribution, ideally a single molecular layer. Before spincoating, we plasma clean the sample for 5 seconds, for surface cleaning and activation. To remove the molecules, the sample is placed in toluene. We use a solution of molecules of one enantiomeric kind at a time.
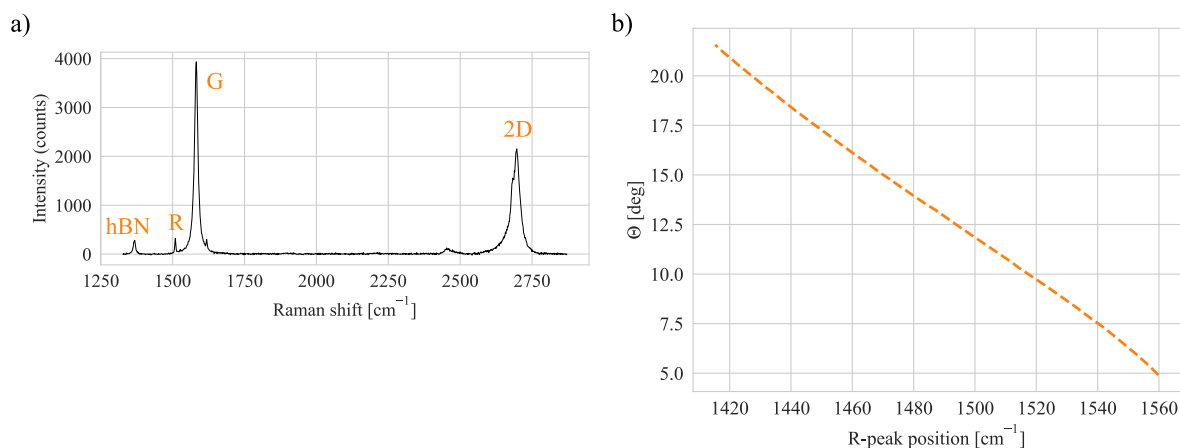
3.2   Sample
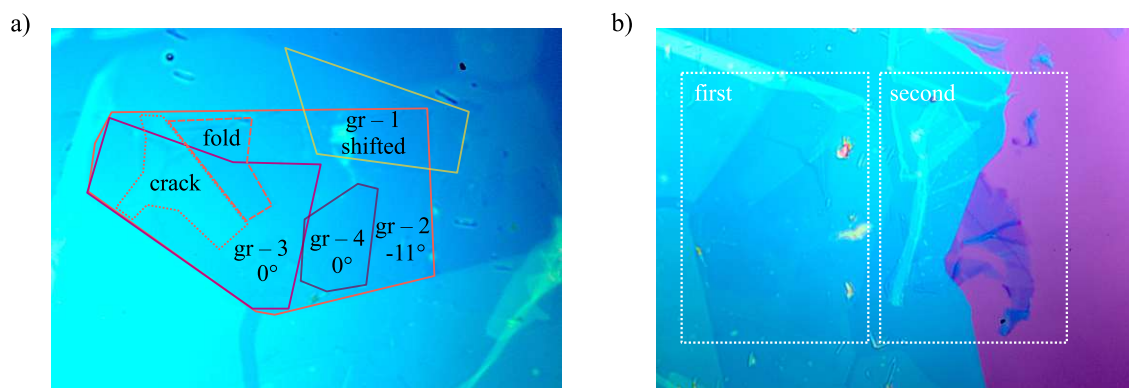
Figure 3.4: *a) Image of the sample, the different graphene areas are marked. Gr - 1 (graphene-1) has shifted while stacking and has an unknown angle. Gr - 2 has a targeted angle of - 11° with respect to gr - 3 and gr - 4. It has a crack, leading to a folded bi- and trilayer area. All graphene areas are encapsulated in hBN. b) Drop of the second part of the sample (right) next to the first part (left), the top hBN is not fully covered by the bottom hBN. Note that the images are rotated with respect to each other and have a different scale.*

Figure 3.4 a) shows the stack done with the lower part of the top hBN flake shown in figure 3.1. The fabrication process followed the procedure described in section 3.1, targeting a twist angle of ± 11°. While stacking the first graphene piece slided, such that it has an asrbitrary angle relative to the second, largest piece of graphene, resulting in a TBG area of unknown angle. A crack in the second piece leads to a fold, with a bi- and a trilayer area. A third and second piece was picked up with a target angle of 0° (corresponding to a twist angle of +11° with respect to the second graphene piece).

All twisted regions shown in a) have the same chirality. For comparison, we would like to have both chiralities on the same sample. We make use of the fact that so far we have only used part of the hBN flake. It is important to use the same top hBN to ensure that the distance between TBG/graphene and the molecules is exactly the same. With the other part of the flake, a TBG stack of the opposite chirality (targeting -11°) is done and dropped onto the same sample, as shown in b).


Figure 3.5: *a) Typical Raman spectrum of TBG, showing the characteristic graphene peaks G and 2D. The relatively small R peak only appears for twisted samples, its position depends on the twist angle. In our sample there is an additional peak associated with hBN. b) Dependence of the R peak position on the twist angle Θ. The data is extracted from [35] and used for estimation of the twist angle from Raman spectral maps.*

Raman spectroscopy is a powerful tool for characterising materials, including graphene, bilayer graphene and TBG. It is used to determine the quality of graphene, the number of layers and orientation. The main Raman peaks in SLG are the G and the 2D peak which are due to in-plane vibrations. The 2D peak is an overtone of the D peak, a peak that only occurs in samples with defects (or near edges) because of momentum conservation (which is satisfied for the 2D peak because it is a two phonon process) and is therefore used to assess the quality of graphene. The 2D peak is closely related to the band structure and changes with the number of layers. For SLG the 2D peak is a single Lorentzian, whereas for BLG it has 4 components [36].

A typical Raman spectrum taken on a TBG area of the sample is shown in figure 3.5 a). In addition to the 2D and G peak, a new Raman band, called R for rotation mismatch, is observed in TBG [37, 38]. The frequency of this superlattice activated Raman peak is associated with a process in which a photo-excited electron is scattered by a phonon with wavevector $\mathbf{q}$. Momentum conservation is ensured through the elastic scattering of the electron by a superlattice wavevector $-\mathbf{q}$ which depends on the twist angle θ. This angle dependence is shown in [35], the data extracted from this plot is shown in figure 3.5 b). This relation allows us to estimate the twist angle from the peak position of the R peak, which we obtain by fitting the corresponding Raman spectrum. For certain excitation energies, strong enhancement of the G and R peaks in TBG, associated with van Hoove singularities, have been reported [35, 39]. We observe such an enhancement of the G peak with a 532 nm excitation laser. However, the quantification of the angle dependence is not straightforward, thus we rely on the relation given by the Raman shift of the R mode.

We observe a Raman peak located at approximately $1366\ \mathrm{cm^{-1}}$ throughout the sample, which is assigned to hBN [40].

a)

b)

c)
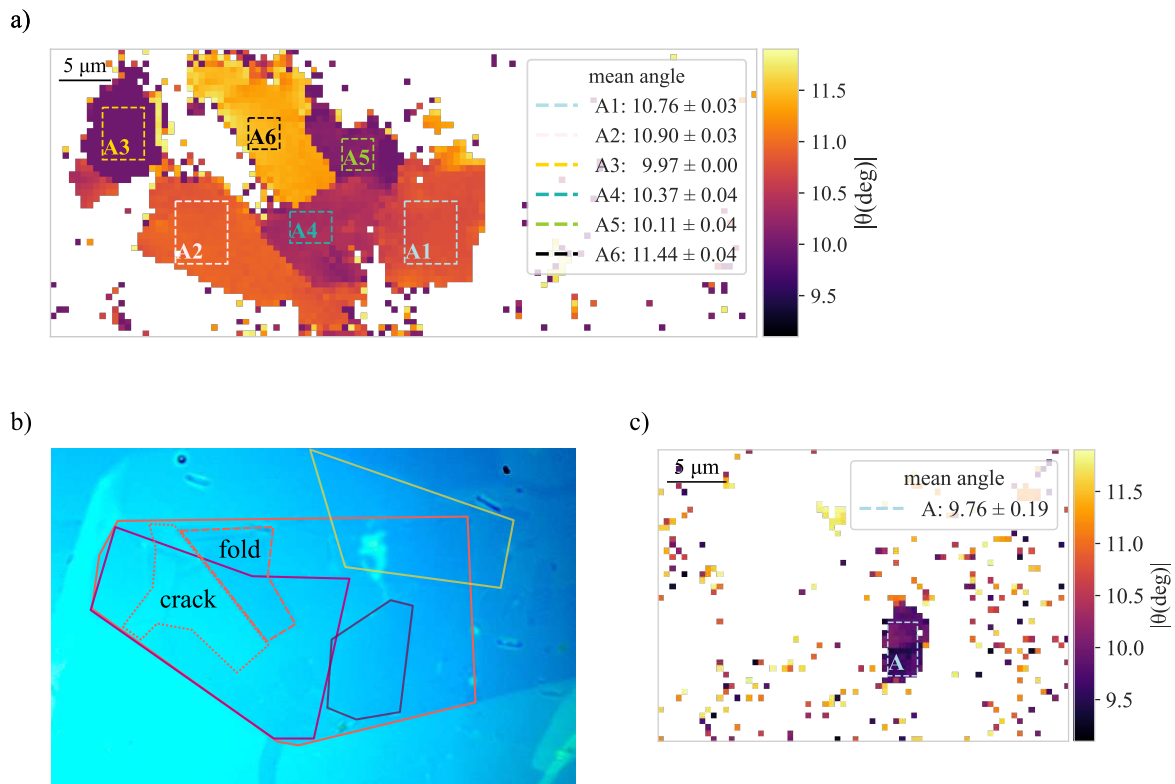
Figure 3.6: a) Spatial variation of the twist angle of the first part of the sample shown in b) for comparison (same as figure 3.4 a)), which corresponds to R-TBG. The angle is estimated by fitting Lorentzians to a spectral Raman map. The position of the R peak is then converted into an angle dependence according to figure 3.5 b). The mean angle of the indicated regions and their corresponding standard deviation are shown. In comparison with b), we can identify regions of different twist angle originating from the cracked and folded graphene flake. The folded part has a slightly higher but similar twist angle. c) There is a small area of homogeneous twist angle with opposite chirality, corresponding to L-TBG. From this analysis we cannot distinguish the sign of the twist angle, so we give the absolute value.

To determine the twist angle, each spectrum of a Raman map is fitted to Lorentzians corresponding to the G, 2D and R peaks. The position of the R peak is then converted into an angle dependence according to figure 3.5 b). The result of this analysis is shown in figure 3.6 a) for the first and b) for the second chirality of TBG. This method only allows to identify the absolute value of the twist angle and not the chirality. By comparing a) with figure 3.4 a), also shown in b) for comparability, we can see that gr-3 has been divided into three or four regions by the crack, which have shifted slightly with respect to each other. Similar to gr-4, these areas have an angle of about 10 to 11 degrees. The folded part also happens to have a similar, slightly larger twist angle (and same chirality). This results in six areas with almost homogeneous angles, between slightly less than 10 and about 11.5 degrees. All these regions have the same chirality. The sample is therefore well suited for analysing the influence of the angle. The other chirality, shown in c) has a small region with a slightly smaller but comparable twist angle, that could

serve as the original objective of comparing the energy transfer for the two chiralities and thus reproduce the preliminary experimental results.

before annealing

a)

b)

after annealing

c)

d)
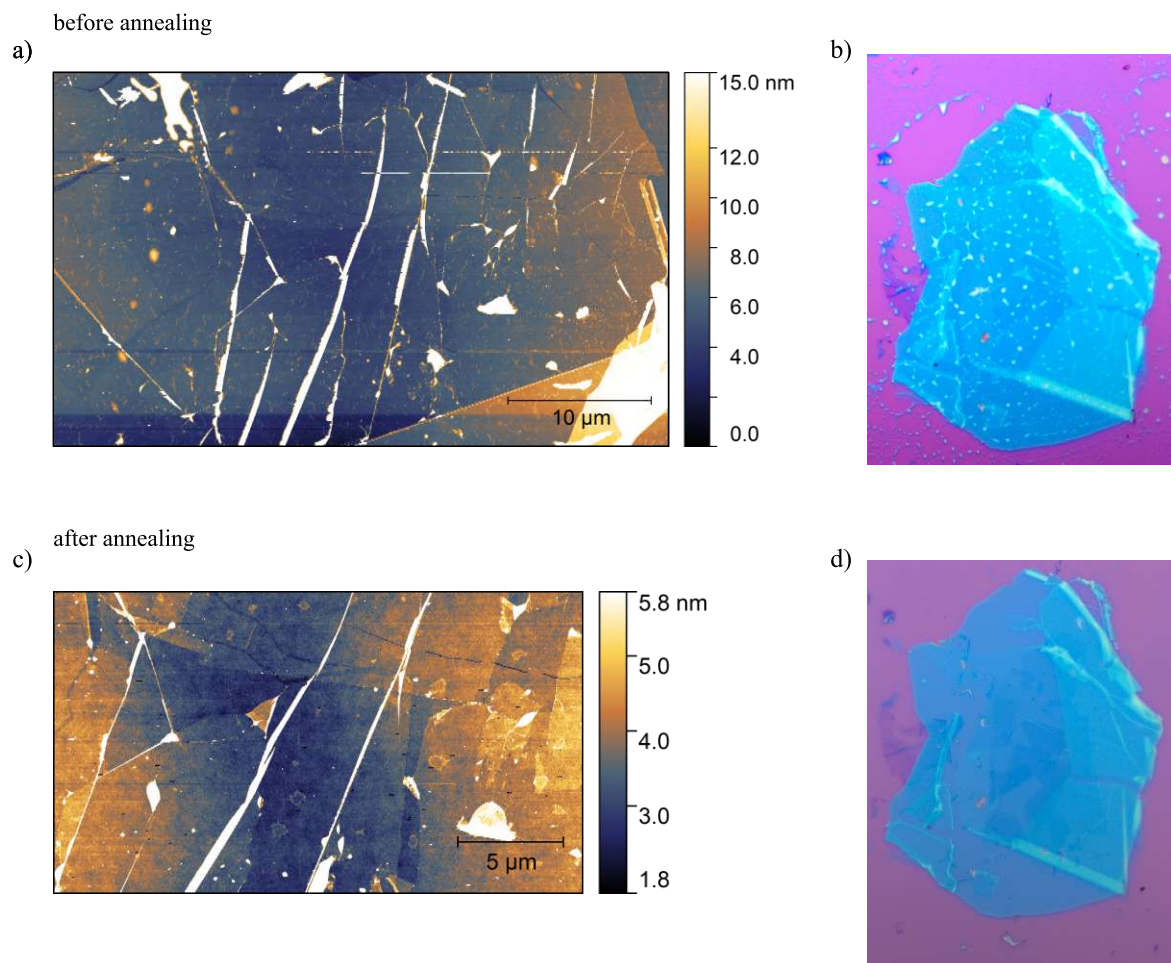
Figure 3.7: *a) and c) AFM images of the sample before and after annealing. The sample looks cleaner after annealing. b) and d) optical image of the sample after spincoating. Before annealing, the molecules formed droplets instead of a uniform film. This is not visible afterwords.*

When trying to spincoat molecules onto the sample, we found that they are not uniformly distributed as they should be, but form droplets, as shown in figure 3.7 b). We associate this with dirt on the surface of the sample, as we had no issues when spincoating on a clean chip. Therefore we clean the sample by vacuum annealing at 400° C for 12 hours with a ramp-up of 100° C/h. When comparing the AFM images of the sample (without molecules) before and after annealing, the surface appears cleaner after annealing. In figure 3.7 a) there is a streaky pattern visible when looking closely, which has disappeared in c). After annealing, the spincoating results in a more uniform film, shown in d), such that the sample is ready to be measured.

4 Conclusion and Outlook

In this report we discussed the energy transfer from chiral molecules to TBG and the associated dissymmetry. We showed that, electromagnetic simulations are able to capture the expected effect. When comparing the simulations to first experimental results and theoretical calculations, we find that the simulated dissymmetry factor is with $g \sim 10^{-6}$ smaller than the theoretically expected ($g \sim 10^{-5}$). This discrepancy might be due to numerical dissipation. Consequently, we conclude that the simulations and theoretical calculations are in agreement. However, this does not resolve the discrepancy between experimental and theoretical results. The large experimental dissymmetry of $g \sim 0.1$ was the main motivation for conducting simulations, aimed at providing further insights. The remaining difference in the order of magnitude, suggests that further investigation is needed to fully understand the effect and its origin. Nevertheless, the occurrence of the effect is confirmed by simulations. We find consistent results, indicating that $g \sim \sigma_{xy}$ which meets our expectation.

To analyze the distance behavior, we first compared the modified decay rate $\Gamma/\Gamma_0 \sim P/P_0$ for short distances and observed a dependence close to the theoretically expected $\sim d^{-4}$, which is typical for energy transfer to two dimensional materials. In contrast, the dissymmetry factor shows a different dependence, clearly separating into two distinct regimes (within the simulated distances between 4 and 80 nm). Up to 20 nm, g decreases slowly with about $d^{-1/3}$. This suggests the potential for long range chiral interactions, opening opportunities for coupling with other technologies. However, for larger distances the dissymmetry decreases significantly, following an approximate d^{-5} dependence. Thus a change in distance behavior is observed around 20 nm, raising questions about the underlying cause of the trend. Further theoretical and experimental investigations into the distance dependence could provide valuable insights into this phenomenon.

Experimentally, we have presented a sample suitable for repeating the measurements on a different device, since confirming the very strong chiral interaction would validate first experimental results. Moreover, the sample enables investigation of the dependence of the dissymmetry on the twist angle, owing to its regions with similar but slightly varying twist angles. In the next step, measurements will be conducted on the sample. To ensure completeness, this will be performed for one enantiomer and repeated for the other. Between the measurements, the sample will be cleaned and spin-coated with molecules of opposite chirality. From the collected data, the molecular lifetimes in the respective regions of the sample can be extracted. Because of quenching, these lifetimes are very short; therefore precise analysis and fitting procedures are required. The dissymmetry factor can then be determined from these results and subsequently compared.

Overall, this project contributes to the investigation of chiral coupling between molecules and TBG and its potential use in sensing. The results open possibilities for further steps, such as studying the distance or angle dependence. It is an important step in improving the understanding of chiral energy transfer and helps in developing a platform for enantiomeric sensing.

5 Appendix

Table 6: *DFT calculations of chiroptical properties of an isolated HBNG1 molecule.*

Wavelength (nm)	State	$|\mu|$ (10^{-20} esu·cm)	$|m|$ (10^{-20} erg/Gauss)	$\cos(\alpha)$	g_{CPL}
631.2	1	295.893	1.466	-0.243	0.0048
563.8	2	431.066	2.341	0.560	-0.0121
531.1	3	222.567	1.213	0.606	-0.0132
519.7	4	205.139	0.924	0.246	-0.0044
503.8	5	95.825	0.980	-0.244	0.0100
497.7	6	92.958	0.839	0.546	-0.0196

Table 7: *DFT calculations of chiroptical properties of an HBNG1 molecule relaxed on hBN.*

Wavelength (nm)	State	$|\mu|$ (10^{-20} esu·cm)	$|m|$ (10^{-20} erg/Gauss)	$\cos(\alpha)$	g_{CPL}
653.9	1	200.961	1.261	-0.099	0.0025
582.7	2	337.017	2.566	0.673	-0.0204
561.1	3	342.252	1.311	-0.175	0.0027
542.6	4	135.478	0.747	-0.312	0.0069
516.5	5	94.630	0.872	0.261	-0.0096
509.0	6	109.116	0.354	-0.578	0.0075

Table 8: *Dissymmetry factor g for different multiplication factors of σ_{xy}, summarized in table 3.*

Multiplication factor of σ_{xy}		$\cdot 10^3$	$\cdot 10^2$	$\cdot 10^1$	$\cdot 1$
$+\sigma_{xy}$	P_+ (nW)	2.364303	1.542159257741	1.535651054426	1.536599956403
	P_- (nW)	2.34590	1.540545036648	1.53549068373	1.536583718609
	g	-0.003907050	0.00052363799	$-5.2218591\cdot10^{-5}$	$-5.28370\cdot10^{-6}$
$-\sigma_{xy}$	P_+ (nW)	2.34547	1.5405059989	1.53656851189	1.536583791767
	P_- (nW)	2.363871	1.5421219421	1.536729779171	1.536599826399
	g	0.00390734	0.00052420958	$5.24736\cdot10^{-5}$	$5.217596\cdot10^{-6}$

Table 9: *Summary of simulation parameters.*

	dipole near a planar interface (section 2.3.1)	dipole near a graphene (section 2.3.2)	dipole near a TBG (section 2.4)	circular dichroism (section 2.3.4)
sphere radius [nm]	1	1	3.5	/
electric dipole	p_x=1	p_x=1	p_z (table 7)	/
magnetic dipole	/	/	p_z (table 7)	/
boundary conditions	scattering	scattering	scattering	scattering, (floquet) periodic
PML thickness [nm]	300	300	300	300
box size [nm]	1200×1200	1200×1200	300×300 (600×600)	300×2400
other domains [nm]	for mesh: 150×150	slab: 0.7 to 30 for mesh: 200×200; 100×100	slab: 0.7 for mesh: 8×8 (2·d×2·d)	slab: 2 for mesh: 300×300, 600×600
λ [nm]	600	600	653 (550 to 790)	550 to 760
materials	air: $\epsilon_1 = \mu_1 = 1$ aluminum: $\epsilon_2 = -32.607$, $\sigma = 8.4143\omega\epsilon_0$	air: $\epsilon_1 = \mu_1 = 1$ hBN: $\epsilon_2 = 4.98$ graphene: $\sigma_\parallel = \sigma_{gr}, \sigma_\perp = 0$	air: $\epsilon_1 = \mu_1 = 1$ hBN: $\epsilon_2 = 4.98$ TBG (see main text)	air: $\epsilon_1 = \mu_1 = 1$ TBG (see main text)
mesh (max size [nm])	sphere: 0.5 box: $\lambda/7$ boundary: $\lambda/30$ PML: 300/5 other: 2	sphere: 0.5 box: $\lambda/7$ slab: 10; 5 PML: 300/5 other: 1	sphere: 0.5 box: 30 slab: 2; 1 PML: 300/8 other: 1	box: 60 slab: 5 PML: 300/5 other: 15; 30

References

1. Lininger, A. *et al.* Chirality in Light-Matter Interaction. *ADVANCED MATERIALS* **35,** 2107325 (2023).

2. Nguyen, L. A., He, C.-h. & Pham-Huy, C. Chiral Drugs: An Overview. *International Journal of Biomedical Science : IJBS* (2006).

3. Barron, L. D. *Molecular Light Scattering and Optical Activity* 2nd ed. (Cambridge University Press, Cambridge, 2004).

4. Kuhn, W. The physical significance of optical rotatory power. *Transactions of the Faraday Society* **26,** 293–308 (1930).

5. Meskers, S. C. J. Circular Polarization of Luminescence as a Tool To Study Molecular Dynamical Processes. *ChemPhotoChem* **6,** e202100154 (2022).

6. Moreno, Á. *et al. Twisted bilayer graphene for enantiomeric sensing of chiral molecules* 2024. arXiv: 2409.05178.

7. Warning, L. A. *et al.* Nanophotonic Approaches for Chirality Sensing. *ACS Nano* **15,** 15538–15566 (2021).

8. Zhao, Y. *et al.* Chirality detection of enantiomers using twisted optical metamaterials. *Nature Communications* **8,** 14180 (2017).

9. Cavicchi, L. *et al. Recognizing molecular chirality via twisted 2D materials* 2024. arXiv: 2409.05839.

10. Novoselov, K. S. *et al.* Electric Field Effect in Atomically Thin Carbon Films. *Science* **306,** 666–669 (2004).

11. Castro Neto, A. H., Guinea, F., Peres, N. M. R., Novoselov, K. S. & Geim, A. K. The electronic properties of graphene. *Reviews of Modern Physics* **81,** 109–162 (2009).

12. Nair, R. R. *et al.* Fine Structure Constant Defines Visual Transparency of Graphene. *Science* **320,** 1308–1308 (2008).

13. Kuzmenko, A. B., van Heumen, E., Carbone, F. & van der Marel, D. Universal Optical Conductance of Graphite. *Physical Review Letters* **100,** 117401 (2008).

14. Novotny, L. & Hecht, B. *Principles of Nano-Optics* 2nd ed. (Cambridge University Press, Cambridge, 2012).

15. Gaudreau, L. *et al.* Universal Distance-Scaling of Nonradiative Energy Transfer to Graphene. *Nano Letters* **13,** 2030–2035 (2013).

16. Morell, E. S., Chico, L. & Brey, L. Twisting dirac fermions: circular dichroism in bilayer graphene. *2D Materials* **4,** 035015 (2017).

17. Moon, P. & Koshino, M. Optical absorption in twisted bilayer graphene. *Physical Review B* **87,** 205404 (2013).

18. Li, G. *et al.* Observation of Van Hove singularities in twisted graphene layers. *Nature Physics* **6,** 109–113 (2010).

19. Kim, C.-J. *et al.* Chiral atomically thin films. *Nature Nanotechnology* **11,** 520–524 (2016).

20. Kim, K. *et al.* Raman Spectroscopy Study of Rotated Double-Layer Graphene: Misorientation-Angle Dependence of Electronic Structure. *Physical Review Letters* **108,** 246103 (2012).

21. Stauber, T., Low, T. & Gómez-Santos, G. Chiral Response of Twisted Bilayer Graphene. *Physical Review Letters* **120,** 046801 (2018).

22. Yang, L. *et al.* Helical Bilayer Nonbenzenoid Nanographene Bearing a [10]Helicene with Two Embedded Heptagons. *Angewandte Chemie International Edition* **62,** e202216193 (2023).

23. *COMSOL - Software for Multiphysics Simulation* https://www.comsol.com/ (2024).

24. Nesterov, M. L., Yin, X., Schäferling, M., Giessen, H. & Weiss, T. The Role of Plasmon-Generated Near Fields for Enhanced Circular Dichroism Spectroscopy. *ACS Photonics* **3,** 578–583 (2016).

25. Mohammadi, E., Raziman, T. V. & Curto, A. G. Nanophotonic Chirality Transfer to Dielectric Mie Resonators. *Nano Letters* **23,** 3978–3984 (2023).

26. Mohammadi, E. *et al.* Nanophotonic Platforms for Enhanced Chiral Sensing. *ACS Photonics* **5,** 2669–2675 (2018).

27. Xiong, H. *et al.* Ultra-thin and broadband tunable metamaterial graphene absorber. *Optics express* **26,** 1681–1688 (2018).

28. Huang, Y. *et al.* Reliable Exfoliation of Large-Area High-Quality Flakes of Graphene and Other Two-Dimensional Materials. *ACS Nano* **9,** 10612–10620 (2015).

29. Diez-Merida, J. *et al.* *High-yield fabrication of bubble-free magic-angle twisted bilayer graphene devices with high twist-angle homogeneity* 2024. arXiv: 2405.11323[cond-mat].

30. Roddaro, S., Pingue, P., Piazza, V., Pellegrini, V. & Beltram, F. The Optical Visibility of Graphene: Interference Colors of Ultrathin Graphite on SiO2. *Nano Letters* **7,** 2707–2710 (2007).

31. Golla, D. *et al.* Optical thickness determination of hexagonal boron nitride flakes. *Applied Physics Letters* **102,** 161906 (2013).

32. Castellanos-Gomez, A. *et al.* Deterministic transfer of two-dimensional materials by all-dry viscoelastic stamping. *2D Materials* **1,** 011002 (2014).

33. Wang, L. *et al.* One-Dimensional Electrical Contact to a Two-Dimensional Material. *Science* **342,** 614–617 (2013).

34. Pizzocchero, F. *et al.* The hot pick-up technique for batch assembly of van der Waals heterostructures. *Nature Communications* **7,** 11894 (2016).

35. Carozo, V. *et al.* Resonance effects on the Raman spectra of graphene superlattices. *Physical Review B* **88,** 085401 (2013).

36. Ferrari, A. C. & Basko, D. M. Raman spectroscopy as a versatile tool for studying the properties of graphene. *Nature Nanotechnology* **8,** 235–246 (2013).

37. Carozo, V. *et al.* Raman Signature of Graphene Superlattices. *Nano Letters* **11,** 4527–4534 (2011).

38. Campos-Delgado, J., Cançado, L. G., Achete, C. A., Jorio, A. & Raskin, J.-P. Raman scattering study of the phonon dispersion in twisted bilayer graphene. *Nano Research* **6,** 269–274 (2013).

39. Havener, R. W., Zhuang, H., Brown, L., Hennig, R. G. & Park, J. Angle-Resolved Raman Imaging of Interlayer Rotations and Interactions in Twisted Bilayer Graphene. *Nano Letters* **12,** 3162–3167 (2012).

40. Cai, Q. *et al.* Raman signature and phonon dispersion of atomically thin boron nitride. *Nanoscale* **9,** 3059–3067 (2017).